

# Thwaites Glacier thins and retreats fastest where ice-shelf channels intersect its grounding zone

## Basal channels, ice thinning and grounding zone retreat at Thwaites Glacier, West Antarctica

Allison M. Chartrand<sup>1,2</sup>, Ian M. Howat<sup>3</sup>, Ian R. Joughin<sup>4</sup>, Benjamin Smith<sup>4</sup>

<sup>1</sup>Earth System Science Interdisciplinary Center, University of Maryland, College Park, MD, USA

<sup>2</sup>NASA Goddard Space Flight Center, Greenbelt, MD, USA

<sup>3</sup>Byrd Polar and Climate Research Center, Ohio State University, Columbus, OH, USA

<sup>4</sup>Applied Physics Laboratory, University of Washington, Seattle, WA, USA

Correspondence to: Allison M. Chartrand (allison.chartrand@gmail.com or nasa.gov)

**Abstract.** Antarctic ice shelves buttress the flow of the ice sheet, ~~tempering sea level rise,~~ but they are vulnerable to increased basal melting from contact with the a warming ocean and, as well as increased mass loss from due to fracture and calving due to changing flow patterns. Melt channels and similar features at the bases of ice shelves have been linked to enhanced basal melting and observed to intersect the grounding zoneline, where the greatest melt rates are often observed. The ice shelf of Thwaites Glacier is especially vulnerable to basal melt and grounding-zone subsequent retreat of the grounding line because the glacier has a retrograde inland-sloping bed leading to a deep trough below the grounded ice sheet. We use digital surface models from 2010–2022 to investigate the evolution of its ice-shelf basal channels, and a proxy for the grounding zoneline position, and the interactions between them on the Thwaites Glacier ice shelf. We find that the highest sustained rates of grounding-zoneline retreat (up to 0.7 km yr<sup>-1</sup>) are associated with high basal melt rates (up to ~250 m yr<sup>-1</sup>) and are found where ice-shelf channels near the intersections of basal channels with the grounding zone, especially atop steep local retrograde slopes, and where subglacial channel discharge is expected. We find no areas with sustained grounding zone advance, although some secular retreat was distal from ice-shelf channels. Pinpointing other locations with similar risk factors could focus assessments of vulnerability to grounding zone retreat. Detailed observations of basal channels co-located with regions of grounding line retreat will further elucidate the complicated processes occurring at the ice-ocean interface and improve hopefully lead to more accurate estimates of current and future ice-shelf melting and evolution.

## 1 Introduction

Thwaites Glacier in the Amundsen Sea region of West Antarctica has the potential to contribute up to 65 cm of sea-level rise (Rignot et al., 2019; Morlighem et al., 2020) and has experienced recent speed-up, ice shelf break-up, thinning, and

Commented [1]: Ed: "melt channels" is not an ideal term b/c there are number of ice-shelf channels with sections of little to no basal melting.

Commented [2]: Ed: line 14: "ice-shelf basal channels" probably means the same thing as "melt channels" and should hence have the same terminology. I suggest to use "ice-shelf channels" throughout.

28 grounding-line retreat (e.g. dos Santos et al., 2021). ~~Thwaites Glacier~~The glacier lies atop an inland-sloping (retrograde)  
29 bed leading to a deep trough reaching 1.5 km below sea level (Morlighem et al., 2020). ~~The glacier terminates in two distinct~~  
30 ~~ice shelves, the Thwaites Eastern Ice Shelf (TEIS) and the Thwaites Western Ice Tongue (TWIT), collectively referred to as~~  
31 ~~the Thwaites Glacier Ice Shelf (TGIS)~~. Several studies have suggested that the Thwaites Glacier grounding zone (GZ, the  
32 region where the ice transitions from grounded to freely floating), may already be undergoing rapid, unstable retreat (Joughin  
33 et al., 2014; Goldberg et al., 2015; Rignot et al., 2014; Yu et al., 2018), in a process known as “marine ice sheet instability”,  
34 or MISI (Gudmundsson et al., 2012; Schoof, 2007; Weertman, 1974). Much of the basal melting and ~~grounding zone~~GZ retreat  
35 is attributed to ~~contact with warm enhanced-ocean melting water~~ (Bevan et al., 2021; Schmidt et al., 2023; Holland et al., 2023)  
36 and loss of basal traction ~~inland upstream~~ of the ~~grounding zone~~GZ (Joughin et al., 2024). ~~Recent evidence suggests that tidal~~  
37 ~~flexure allows seawater to intrude into the embayed grounding zone in the main trunk of the TWIT (located within Box C in~~  
38 ~~Figure 1), which may accelerate melting below intermittently grounded ice (Rignot et al., 2024). The TWIT has weakened~~  
39 ~~rapidly over the past several decades (e.g. Miles et al., 2020), and the TEIS is expected to weaken significantly in the coming~~  
40 ~~decades (e.g. Wild et al., 2022).~~

41 Several studies have shown that high rates of ice-shelf thinning and basal melting are often associated with ice-  
42 shelf basal-channels, which are curvilinear incisions at the ice-shelf base believed to be maintained by buoyant meltwater  
43 plumes entrained within them along-flow (Alley et al., 2016; Drews, 2015; Chartrand and Howat, 2020; Gourmelen et al.,  
44 2017; Wearing et al., 2021) Others have shown that ~~ice-shelf basal~~ channels are also commonly associated with ice-shelf  
45 weakening through fracturing as a result of thinning (Vaughan et al., 2012; Dow et al., 2018; Alley et al., 2019). ~~Ice-shelf Basal~~  
46 channels initiate at the grounding ~~line zone~~ and extend seaward. ~~They often represent advected extensions of inverted troughs~~  
47 ~~initiated by subglacial channelization beneath the grounded ice or may be incised by undulations in the bed (e.g. Le Brocq et~~  
48 ~~al., 2013; Alley et al., 2016; Drews et al., 2017). Where they represent extensions of subglacial channelization is presents, the~~  
49 ~~input of fresh subglacial meltwater may contribute to the growth of a buoyant they are likely formed by a meltwater plume that~~  
50 ~~can entrain warm ocean water as it travels along the ice-shelf channel, enhanced by the fresh glacial outflow (Jenkins, 2011).~~  
51 ~~However, it remains difficult to attribute the formation mechanism to any given channel, particularly if its surface expression~~  
52 ~~does not intersect the grounding zone (e.g. Alley et al., 2016; Chartrand & Howat 2020). The Thwaites Glacier Ice Shelf~~  
53 ~~(TGIS) has at least four previously mapped ice-shelf basal channels (Alley et al., 2016) and the grounded ice is underlain by at~~  
54 ~~least two persistent subglacial channels intersecting the grounding zone GZ (Hager et al., 2022). Recently, subglacial channels~~  
55 ~~and aligned ice-shelf basal channels on Greenland ice tongues have been linked to thinning and retreat of the grounding line~~  
56 ~~(Ciraci et al., 2023; Narkevici et al., 2023). It is unknown, however, the extent to which ice-shelf basal channels on the TGIS~~  
57 ~~and/or subglacial channels within grounded ice may have contributed to the thinning and retreat at Thwaites Glacier.~~

58 In the absence of a method for directly measuring ice thickness from space, observations of ~~ice-shelf basal~~ channels  
59 and channel-like features (i.e. ~~ice-shelf basal~~ incisions oriented predominantly along-flow without clear evidence of  
60 subglacial initiation or entrained meltwater flow) and their relationship to variations in ~~grounding zone~~GZ position and other  
61 ice-shelf structures are only available from ~~high-resolution (<100 m) precise~~ measurements of surface height. While relatively  
2

Commented [3]: R2 It is unclear here what the relative role of subglacial channelization and meltwater plumes is in creating these ice shelves basal channels.

Commented [4]: Ed: line 47: "precise" --> "high-resolution (<100 m)"

frequent and accurate, observations from spaceborne altimetry, such as ICESat and ICESat-2, are limited to ground tracks. Recently, high-resolution digital surface models (DSMs) produced from stereoscopic satellite imagery, combined with altimetry, have been used to map changes in ice-shelfbasal channels and other ice-shelf structures (Chartrand and Howat, 2020; Shean et al., 2019; Zinck et al., 2023). Using the extensive collection of repeat DSMs provided by the Reference Elevation Model of Antarctica (REMA) project (Howat et al., 2019), we map the positions of surface depressions overlying ice-shelfbasal channels on the TGIS and subglacial channels within grounded ice as well as the landward extent of the transition to flotation as a proxy for the grounding line, termed the hydrostatic boundary (HB). We also construct the most comprehensive maps to date of time-evolving surface height, thickness, and basal mass change for the Thwaites Glacier and TGIS. Here we examine the transient locations of the ice-shelfbasal channels relative to those of the HB, as well as to variations in basal melt and flow speed, to assess the potential relationship between channels and grounding-zone retreat.

## 2 Datasets

We use several geophysical datasets for this study as described throughout this section.

### 2.1 REMA Digital Surface Model (DSM) strips and annual mosaics

Reference Elevation Model of Antarctica (REMA) DSMs for the TGIS are obtained through stereophotogrammetry applied to pairs of commercial submeter-resolution, panchromatic satellite images acquired by the MAXAR constellation, including Worldview-1, -2 and -3, Quickbird-1 and -2, and GeoEye satellites (Howat et al., 2019). Elevations from REMA DSMs are relative to the WGS84 ellipsoid and are distributed both as individual “strips” representing WGS84-ellipsoid elevations, created from a single pair of images along their overlapping swath, and as seamless, continuous mosaics made from those strips. Both product types are distributed at 2 m resolution, with downsampled versions available. We use the REMA 200 m mosaic for the Thwaites region as a base map in several figures.

We utilise the DSM strips at 10 m resolution to map the HB (Section 3.1) and ice-shelfbasal channels (Section 3.2). After removing strips with insufficient coverage or low internal quality, as indicated in the metadata by a root-mean-squared error value greater than 1 m, there are 191 strips for the TGIS.

We combine REMA strips into full-coverage (depending on strip availability) annual mosaics at 50 m resolution to compute rates of change across the TGIS (Section 3.3). As strips are more readily available for summer months, REMA strips from November to March are mosaicked to form an austral annual mosaic, for which we assign a nominal date of January 1. For each annual mosaic, each strip is co-registered to every other using the method of Nuth and Kaab (2011). The co-registered strips are then stacked, and the annual mosaic is the median height at each pixel through the stack (Fig. S1).

As part of this process, each strip and annual mosaic is registered to correct for single-value elevation biases using ICESat-2, CryoSat-2, or Operation IceBridge (henceforth, IceBridge) altimetry data, depending on availability and/or which dataset is temporally closest to the collection date of the strip. The registration dataset selected is based on a hierarchy; if the

93 first dataset is unavailable, the next dataset will be used, and so on. Priority is given to overlapping ICESat-2 ATL06 Version  
94 5 (Smith et al., 2021) or Version 6 (Smith et al., 2023) ground control points (GCPs) that were collected within 10 days of the  
95 strip or 100 days of the annual mosaic nominal date, then to GCPs from the ICEBridge Airborne Topographic Mapper (ATM)  
96 L1B (Studinger, 2013), the IceBridge Land, Vegetation, and Ice Sensor (LVIS) L2 (Blair and Hofton, 2015), or the IceBridge  
97 and ICECAP Riegl Laser Altimeter L2 (Blankenship et al., 2012) datasets collected within 10 or 100 days. Strips with no  
98 contemporaneous ICESat-2 or IceBridge GCPs were registered to CryoSat-2 SAR-In mode elevations (European Space  
99 Agency, 2023) collected within about 365 days of the strip. Unlike ICESat-2 and IceBridge registrations which register the  
100 strip to temporally proximal GCPs, the CryoSat-2 registration is determined by a linear fit to elevation differences with respect  
101 to time so that the DSM is fit to a temporal model of the elevation data. Strips that do not meet these registration criteria are  
102 eliminated, leaving 177 strips over the TGIS (Fig. S2).

103 The strips and annual mosaics are not smoothed, but they are masked to remove artefacts and errors like clouds.  
104 Following registration, the absolute residual, and mean and standard deviation thereof, between each DSM and the REMA  
105 mosaic is computed. Then, the residual is smoothed by a 50 pixel (500 m for strips or 2500 m for annual mosaics) moving  
106 mean, and any DSM pixels that correspond to a smoothed residual that is 2–5 standard deviations greater than the mean residual  
107 are masked out; a larger magnitude in the residual mean or standard deviation triggers a smaller standard deviation threshold  
108 for that strip. These thresholds were chosen to effectively remove artefacts and errors like clouds, but to maintain differences  
109 due to the advection of surface features.

110 Following the procedure in Chartrand and Howat (2020), registered and masked strip and annual mosaic ellipsoid  
111 elevations are converted to freeboard heights ( $h$ ) by referencing to mean sea level using the EIGEN-6C4 geoid model (Förste  
112 et al., 2014), correcting for Mean Dynamic Topography using the DTU22 MDT model (Knudsen et al., 2021), accounting for  
113 firm density, and correcting for tidal variations using the CATS2008b inverse tide model (Padman et al., 2018).

## 114 2.2 BedMachine Antarctica

115 Bed heights referenced to the geoid are obtained from BedMachine Antarctica, Version 3 (Morlighem, 2022). The BedMachine  
116 bed heights and grounded ice thicknesses are used to estimate subglacial conditions (Section 3.4). This dataset also contains  
117 masks for floating ice, grounded ice, ice-free land, and ocean which are used to select strips based on their overlapping area  
118 with the relevant masks.

## 119 2.3 Ice velocities

120 Ice surface velocity for the TGIS is obtained from NASA Making Earth System Data Records for Use in Research  
121 Environments (MEaSUREs) mosaicked, 450 m resolution posting, InSAR-Based Antarctic Ice Velocity Map, Version 2  
122 (henceforth, “velocity mosaic”; Mouginit et al., 2012; Rignot et al., 2011, 2017), the MEaSUREs 1 km posting, SAR-Based  
123 Annual Antarctic Ice Velocity Maps, Version 1 (henceforth, “annual velocity maps”; Mouginit et al., 2017a), and 250 m

Commented [5]: R2 SAR-In -> SARIn

Commented [6]: Ed: line 95: Is firm density not relevant for the hydrostatic correction? (I only now see that this is done in 3.1)

Commented [7]: Ed: The grounding thickness in Bedmachine is not well-defined.



posting ~~quarterly-velocity maps for the austral summer quarters (Oct-Dec and Jan-Mar)~~ velocities that we derived using speckle tracking applied to Sentinel 1 A/B images from TGIS and Pine Island Glacier. The 450 m posting MEaSURES mosaic is used to obtain masks for ice moving  $< 20 \text{ m yr}^{-1}$  for registering strips and for filtering the annual and quarterly velocity maps. The MEaSURES annual velocity maps obtained for 2011–2015 are variable in their spatial coverage and quality, while the quarterly velocity maps obtained for 2016–2023 have more consistent coverage and better quality. ~~so for~~ To obtain annual velocity maps from 2011–2023 with more consistent quality, we initially take different approaches to filling data gaps and reducing noise in each dataset: for the 2011–2015 annual velocity maps, we take the average of each annual map and the velocity mosaic at each pixel; each year we take the ~~median of each the annual map and the average velocity map.~~ The quarterly velocity maps obtained for 2016–2023 have more consistent coverage and better quality. For consistency in temporal resolution throughout the study period, for the 2016–2023 quarterly maps, we take the average of each year's independently stack the ~~we take the median of the two Oct-Dec map and Jan-Mar (austral summer) quarterly maps at each pixel for each year of the 2016-2023 data.~~ Each resulting filled, noise-reduced annual map from the whole study period is then bilinearly interpolated to the same grid as the annual REMA mosaics and further filtered by taking the median velocity and standard deviation at each pixel throughout the time period and masking out pixels in each year where the velocity differs from the median pixel velocity by more than 2.5x the standard deviation for that pixel, then smoothing the velocity for each year with a 600 m moving mean window. The annual velocity maps are used to flow-shift the annual DSM mosaics to obtain Lagrangian rates of change and to investigate changes in velocity where we observe rapid ~~HB~~ grounding-line retreat.

#### 2.4 Historical grounding lines and calving front

Historical grounding lines are obtained from the MEaSURES Antarctic Grounding Line from Differential Satellite Radar Interferometry, Version 2 for 7 February 1992 to 17 December 2014 (Rignot et al., 2016). Furthermore, ~~the~~ grounding line from the MEaSURES Antarctic Boundaries for the 2007–2009 International Polar Year (IPY) from Satellite Radar, Version 2 dataset (Mouginot et al., 2017b) is ~~also~~ used as a reference grounding line from which to measure changes in the grounding zone position and is henceforth termed 07–09 IPY GL or simply IPY GL. This dataset provides ~~to obtain~~ a complete and continuous grounding line ~~derived from a variety of satellite platforms.~~ ~~(henceforth termed 07–09 IPY GL or simply IPY GL).~~ Additional historical grounding lines are obtained for a long term visual comparison (Fig. 1) from the MEaSURES Antarctic Grounding Line from Differential Satellite Radar Interferometry, Version 2 for 7 February 1992 to 17 December 2014 (Rignot et al., 2016); however these are not used for analyses.

### 3 Methods

We use a variety of previously defined and novel techniques to investigate changes on the TGIS, described below.

Commented [8]: R1 which "annual velocity map"?

Commented [9]: R1 how can you have a "median of two" and how do you define "summer quarters"?

Commented [10]: R1 how can you have a "median of two" and how do you define "summer quarters"?

Commented [11]: R2 Could you say more about the 07-09 GL datasets? Is this the 2011 grounding line in <https://agupubs.onlinelibrary.wiley.com/doi/full/10.1002/2014GL060140> ? Which would then tie in nicely with the start of your HB record in 2011.

153 **3.1 Mapping the hydrostatic boundary**

154 The hydrostatic boundary (HB) is defined as the point at which the grounding thickness matches the flotation thickness. The  
155 grounding thickness is the distance between the observed ice surface and the bed from BedMachine. Flotation thickness ( $H_E$ )  
156 is determined from the DSM strip freeboard heights ( $h$ ) as in Chartrand & Howat (2020, 2023):

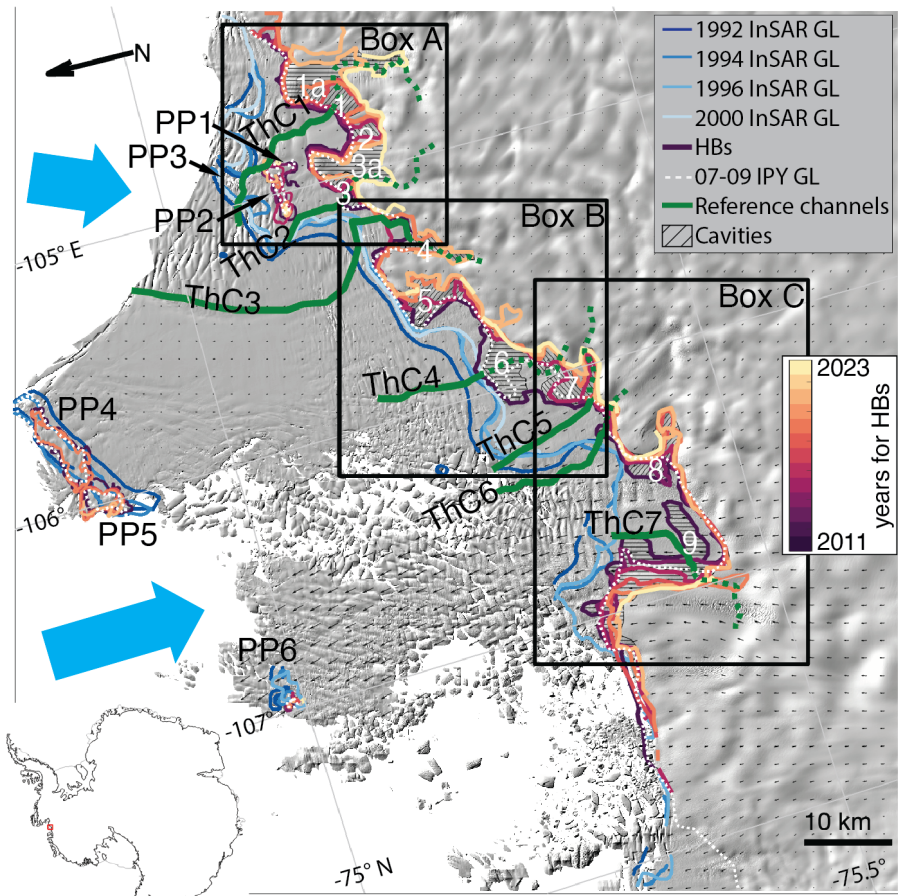
157 
$$H_E = h \frac{\rho_s}{\rho_s - \rho_i} - H_a \frac{\rho_a - \rho_i}{\rho_i - \rho_s} \#(1),$$

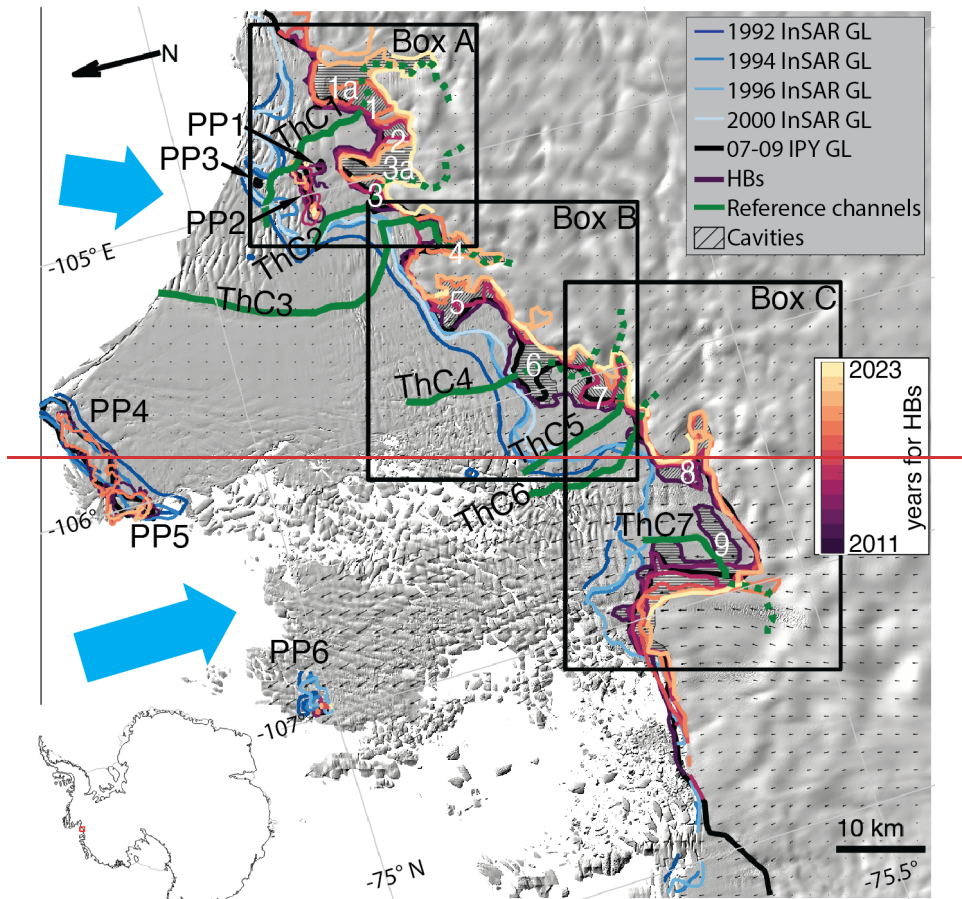
158 where  $\rho_s$  is seawater density ( $1,027 \text{ kg m}^{-3}$ ),  $\rho_i$  is meteoric ice density ( $918 \text{ kg m}^{-3}$ ),  $\rho_a$  is the firm-air column density ( $2 \text{ kg}$   
159  $\text{m}^{-3}$ ), and  $H_a$  is the thickness of the firm-air column within the freeboard (specifically, the length of the change in firm  
160 thickness resulting from compressing the firm column to ice density (Ligtenberg et al., 2011)). The subscript  $E$  denotes that  $H_E$   
161 is an estimate of ice thickness.

162 We use the 07–09 IPY GL as the basis for where HBs are expected to be mapped. We track HBs at ~~each independent,~~  
163 ~~continuous grounding line from the IPY,~~ including the continental grounding line and six pinning points (PPI–6) ~~delineated~~  
164 ~~in the IPY GL.~~ For each strip, the difference between  $H_E$  and the grounding thickness is computed at each pixel. This difference  
165 is converted to a contour map, and the coordinates of pixels that lie on the 0 m contours are stored as features representing  
166 HBs near the continuous IPY GL and each pinning point. These features are filtered and simplified for analysis as follows  
167 (Fig. S3). For each strip, HB features containing fewer than 25 coordinates are removed, and the remaining HB feature  
168 coordinates are smoothed by a 50 point moving mean (a distance of about 200 m). If the strip has coverage over a given  
169 grounding line, a polygon is manually defined to encapsulate the HB features that most likely represent that grounding line  
170 (i.e., the polygon is defined to keep the longest and most continuous HB features and eliminate small isolated HBs), and points  
171 outside of the polygon are eliminated. Then, HB features are combined by year, and an annual HB with a nominal date of  
172 January 1 is manually defined along the most ~~inlandupstream~~ features for the continental GL, and the innermost features for  
173 each pinning point, from each year. ~~The annual HBs and unfiltered HB features are shown as curves with a purple-orange-~~  
174 ~~yellow-colour scale throughout the figures.~~

Commented [12]: R1 please expand what you mean by "each independent continuous grounding line"

Commented [13]: R1 I admire that you have used 'inclusive' colour scales. It is best not to refer to the (subjectively received) colours in the main text but allow the figures to speak for themselves





177  
 178 **Figure 1:** REMA 200 m mosaic hillshade for the Thwaites Glacier and Thwaites Glacier ice shelf (TGIS) overlain by historical  
 179 grounding lines derived from InSAR (curves in shades of blue), the continuous InSAR-derived 07–09 IPY GL (white dashed black  
 180 curve, including pinning points PP1–6), and selected hydrostatic boundaries (HBs) identified in this study (curves in shades of purple,  
 181 orange, and yellow, with lighter shades representing more recent HBs). The reference channels for the ice-shelf basal channels and  
 182 surface depressions identified in this study are shown as solid and dashed green curves, respectively, and labelled ThC1–7. Hatched  
 183 regions indicate cavities that opened as the HB retreated throughout the study period, labelled 1–9. Large blue arrows indicate the  
 184 general location of circumpolar deep water (CDW) inflow to the ice-shelf cavity (Dutrieux et al., 2014). The black boxes, Box A–C,  
 185 indicate the zoomed regions in following figures. Small black arrows represent ice flow.

Commented [14]: R1 The IPY GL and 2011 GL are apparently in the same colour and the former is probably obscured by the HB sequence. Some adjustments (or removals) are required here.

186

### 187 3.2 Mapping ice-shelfbasal channels and surface depressions

188 Complementary methods are used to locate persistent curvilinear ice-shelfbasal basal features, including ice-shelfbasal channels,  
189 as they are not directly observable using surface elevation alone. Sufficiently large ice-shelfbasal channels (usually > 1 km  
190 wide) correspond to surface depressions that are resolvable as stream-like features in the surface topography (Drews, 2015).  
191 We do not attempt to verify the presence of entrained meltwater flow in the basal features we identify, and refer to all  
192 consistently mapped basal incisions that are oriented predominantly parallel to flow and associated with surface depressions  
193 as ice-shelfbasal channels. Ice-shelfBasal channel locations from Alley et al. (2016) are used to initially query REMA DSM  
194 strips.

195 We map surface depressions over both grounded and floating ice by refining the method of using DSM local minima  
196 to map surface depressions (Chartrand and Howat, 2020). We compute maps of hypothetical stream channel depth for the ice-  
197 shelf surface from strip freeboard heights using the flow accumulation (“flowacc”) function from the MATLAB-based  
198 TopoToolbox software (TopoToolbox, 2023). We assume that features with high flow accumulation are surface depressions.  
199 We then compare potential depressions with DSM hill shade renderings, eliminating those that align with clear fractures  
200 (usually perpendicular to flow), are very short (< ~1 km), or do not intersect the ice shelf.

201 To identify ice-shelfbasal channels on the shelf, we compute flotation thickness from strip freeboard height (Eq. 1)  
202 and determine the depth of the hydrostatic ice-shelf draft ( $h - H_E$ ) relative to sea level. We invert the ice-shelf draft by  
203 multiplying its depth by  $-1$ , and again compute the hypothetical stream channel depth and flow accumulation across the  
204 inverted ice-shelf base, with the locations of stream flow identified as possible ice-shelfbasal channels. As for the surface  
205 depressions, we remove spurious features by comparison with DSM hill shade renderings of both the surface and inverted  
206 basal topography.

207 Where available, potential ice-shelfbasal channels are verified using IceBridge and pre-IceBridge MCoRDS L2 ice-  
208 penetrating radar (IPR) thicknesses (Paden et al., 2011, 2010) (Figs. S4–5). If a basal incision and/or surface depression does  
209 not match with a thickness minimum or a previously identified ice-shelfbasal channel (e.g. Alley et al., 2016), we do not rule  
210 out that it could be an ice-shelfbasal channel with entrained meltwater flow and look for other evidence of its formation.

### 211 3.3 Estimating rates of change

212 Time-evolving rates of change are estimated from the annual DSM mosaics within four epochs: 2011–2015, 2016–2019,  
213 2020–2023, and the entire study period from 2011–2023. Within each epoch, rates of change are calculated from all  
214 combinations of annual mosaics such that the relevant quantity derived from the earlier mosaic in each combination is  
215 subtracted from the later mosaic and divided by the time elapsed between the mosaics, in both Eulerian (fixed-coordinate  
216 system, denoted by  $dQ/dr$ , where  $Q$  is the quantity in question) and Lagrangian (coordinate system moves with ice flow,

denoted by  $dQ/dt$  reference frames. The Eulerian reference frame (fixed coordinate system, denoted by  $dQ/dt$ , where  $Q$  is the quantity in question) is used over grounded ice, to prevent slope-induced errors, and the Lagrangian reference frame (coordinate system moves with ice flow, denoted by  $DQ/Dt$ ) is used over floating ice, where height variability change is dominated by horizontal advection. The strip-derived annual HB from each year is used to delineate the extent of floating and grounded ice for each annual mosaic. For grounded ice, we calculate the Eulerian rate of thickness change ( $dH/dt$ ), where grounded ice thickness,  $H$ , is simply the DSM-derived surface height minus the BedMachine bed height. For floating ice, we calculate Lagrangian rates of ice-column surface height change ( $Dh/Dt$ ), thickness change ( $DHE/Dt$ ), where flotation thickness  $HE$  is derived from annual DSM mosaic freeboard heights using Eq. 1, and basal mass loss or gain ( $M_b$ ). For Lagrangian calculations, the mosaics are flow-shifted to a common date using the smoothed annual surface velocity maps (Section 2.3) following the approach of Shean et al. (2019) and Chartrand & Howat (2020). Four epochs are defined: 2011–2015, 2016–2019, 2020–2023, and the entire study period from 2011–2023. The mosaics are flow-shifted to 1 January of the earliest full year in each epoch (e.g., 1 January 2011 for the 2011–2015 epoch and the full study period).

Within each epoch, rates of change are calculated from all combinations of annual mosaics such that the relevant quantity derived from the earlier mosaic in each combination is subtracted from the later mosaic and divided by the time elapsed between the mosaics. For floating ice, we calculate the quantities considered are the rate of ice-column surface height change ( $dh/dt$  for grounded ice and  $Dh/Dt$  for floating ice) and, the rate of thickness change ( $dH/dt$  and  $DHE/Dt$ ), and the Lagrangian rate of basal mass loss or gain ( $M_b$ , for floating ice only). Lagrangian ice-column thinning can occur as a result of stretching as the ice accelerates (dynamic thinning) or as a result of surficial or basal ablation, although these mechanisms cannot be attributed by a calculation of  $DHE/Dt$ , which only reflects how the surface height changes as the column advects due to the hydrostatic assumption. For grounded ice, we calculate the Eulerian rate of thickness change ( $dH/dt$ ), where grounded ice thickness,  $H$ , is simply the DSM-derived surface height minus the BedMachine bed height. The strip-derived annual HB from each year is used to delineate the extent of floating and grounded ice for each annual mosaic.

Flotation thickness  $H_E$  for the TGIS is derived from annual DSM mosaic freeboard heights using Eq. 1. The Lagrangian basal accumulation-mass change rate  $M_b$  (m ice equivalent  $\text{yr}^{-1}\text{a}^+$ , negative values imply basal melt), for floating ice is determined from mass conservation as:

$$M_b = \frac{DH_E}{Dt} + H_E(\nabla \cdot \mathbf{u}) - M_s \quad (2),$$

where  $M_s$  is the surface accumulation rate (m  $\text{yr}^{-1}\text{a}^+$ , positive for mass gain), and  $\nabla \cdot \mathbf{u}$  is the divergence in the column-average horizontal velocity of the ice  $\mathbf{u}$  (m  $\text{yr}^{-1}\text{a}^+$ ). As in Shean et al. (2019), the velocity divergence is computed at each time step prior to flow-shifting the DSM is flow-shifted, so the  $M_b$  estimate accounts for the flow history of each pixel. The rate of surface accumulation for Antarctica is obtained from the Regional Atmospheric Climate Model (RACMO) 3p2 (van Wessem et al., 2018) which provides estimates of  $M_s$  for 1979–2016 on a 27-km grid. We bilinearly interpolate the per pixel mean  $M_s$  from 2011–2016 to the mosaic grid coordinates and convert to ice-equivalent mass change rates. The maps of rates

Commented [15]: Ed: brackets in eq (2) are not correct.

Commented [16]: R2 Should it say “the velocity divergence is computed at each time step prior to the DSM being flow-shifted, ...”?

Commented [17]: R2 What are the implications of having the SMB data only up to 2016 when the melt rate is calculated up to 2023? What would the impact of large anomalies e.g. <https://www.nature.com/articles/s41467-023-36990-3> be?



of change are smoothed by a 500 m moving mean and extreme values resulting from remaining artefacts from clouds or poorly co-registered strips in the annual mosaics are filtered out.

Commented [18]: R1 "Remaining artefacts .. are filtered out". Please elucidate.

### 3.4 Estimating subglacial conditions

To assess potential spatial relationships between the locations where subglacial hydrologic pathways reach the grounding zoneGZ and align with ice-shelf-basal channels, we derive a map of the subglacial hydraulic potential ( $\Phi$ ) based on observations (Fig. S6) as:

$$\Phi = \rho_w g z + \rho_i g H \quad (3),$$

where  $g$  is the acceleration due to gravity and  $z$  and  $H$  are equal to the BedMachine bed height and grounded ice thickness, respectively. Assuming that water is present everywhere at the bed, we again use the TopoToolbox FLOWobj function to compute the direction that water would flow along the gradient of the hydraulic potential, and the flow accumulation ("flowacc") function to find the cumulative number of pixels that contribute to flow in each downstream pixel, and convert this to the cumulative drainage area, or basal watershed area, for each pixel along the hydraulic potential gradient. While not intended as an actual estimate of subglacial discharge, this quantity provides a relative metric of where water is likely to be routed in the subglacial system. We compare spatial patterns in inferred subglacial drainage at the grounding zoneGZ with the occurrence of mapped ice-shelf-basal channels.

### 3.5 Uncertainty and sources of error

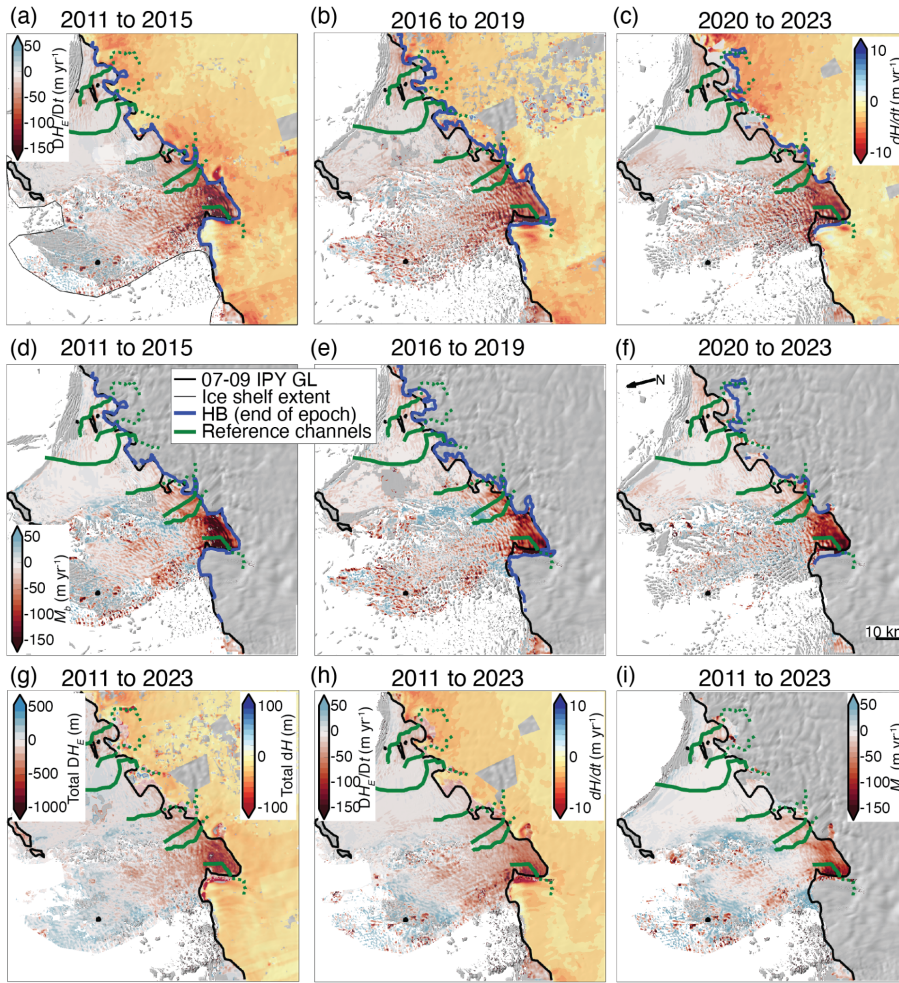
Estimates of rates of changes in surface height, thickness, and basal mass-change are subject to uncertainties in the remotely-sensed measurements, model outputs, and assumptions from which they are derived. Our methods follow those of Chartrand and Howat (2020), which showed that uncertainties in DHE/Dt and Mb range from ~8–22 m yr<sup>-1</sup>; this is similar to the variability in our estimates (Table 1). We note that  $M_s$  is derived from a temporal average of RACMO model output from only part of our study period, which may omit the impact of anomalous precipitation events on our estimates of  $M_b$ . However, as we are interested in the spatial variability of grounding zoneGZ change over several years, we do not expect the omission of short-term, regional events to significantly impact our results as they will be partially captured in DSM surface heights.

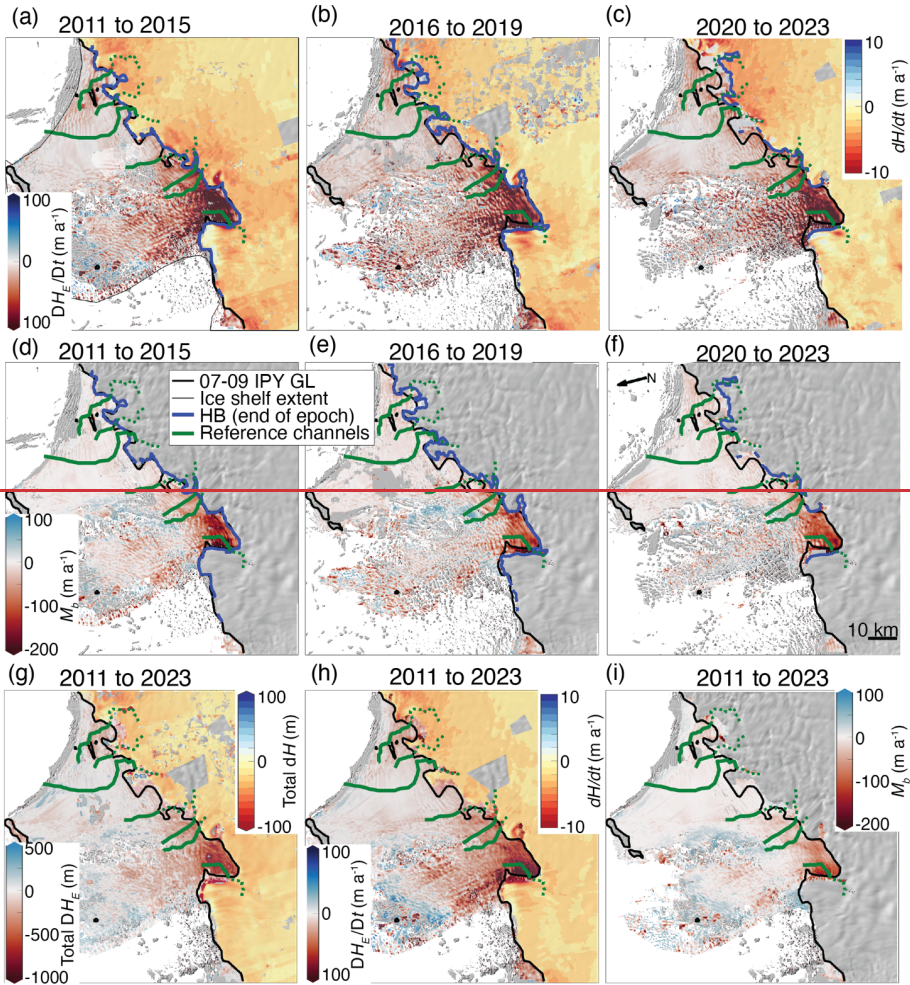
Mapping of ice-shelf channel surface depressions and hydrostatic boundaries is subject to uncertainties arising from the hydrostatic assumption, errors in manual delineation, and errors in the BedMachine bed height (Fig. S8). In particular, the hydrostatic assumption may not be valid for portions of the TGIS (Chartrand & Howat, 2023), and an ice shelf's deviation from hydrostatic balance may vary through time in the vicinity of ice-shelf channels (Chartrand & Howat, 2020; Stubblefield et al., 2023). However, hydrostatic imbalance and temporal variations therein are estimated to be a fraction of ice thickness (e.g. Chartrand & Howat, 2023; Stubblefield et al., 2023), and ~~which is~~ comparable to the BedMachine error in the vicinity and inland of the IPY GL (Fig. S8; Morlighem et al., 2022). As we are interested in relative HB position through time, which occurs over distances longer than ice thickness, rather than absolute HB position, we do not expect hydrostatic imbalance to

280 impact our interpretation of relative HB position inland of the IPY GL. However, the errors in BedMachine bed height increase  
281 rapidly to ~400 m between 2–5 km downstream of the IPY GL, so we are not as confident in absolute or relative HB position  
282 when it is mapped downstream of the IPY GL. Furthermore, it should be noted that the IPY GL is derived from interferometric  
283 SAR imagery and represents the inland limit of ice flexure, whereas the HBs represent the inland limit of hydrostatic balance,  
284 which may differ from the limit of flexure by several km (e.g. Fricker et al., 2009). The IPY GL is therefore used only as a  
285 reference from which to measure HB change, although it is fortuitous that the IPY GL (delineated from data primarily collected  
286 in 2007–2009) represents the grounding line position near the beginning of DSM availability. As described in Section 3.1,  
287 manual input is used to delineate the annual HB for each annual epoch, from which relative position is derived; the raw HB  
288 features are not subject to manual error. Following masking to remove small, isolated HB features from consideration for the  
289 annual HB, points along the most inland HB features from each year are manually selected so that the annual HB consistently  
290 represents the grounding line in its most retreated position; we estimate that this manual delineation introduces independent  
291 errors < 200 m, or 20 DSM strip pixels, in the position of any point along the annual HB.

292 Manual input for the ice-shelf channel surface depression positions is used to filter out spurious depressions in the  
293 TopoToolbox output features, such as those that align with flow-perpendicular crevasses, and to define the reference channel  
294 positions based on where a channel was consistently mapped by TopoToolbox in many DSMs. Thus, the reference channel  
295 positions represent a manually-defined “average” of each ice-shelf channel’s position through time and may not reflect its  
296 position at any given time.







298  
 299 **Figure 2:** (a–c) Median Lagrangian rate of thickness change ( $DH_E/Dt$ ) on floating ice (dark red to blue colour scale) and Eulerian  
 300 rate of thickness change ( $dH/dt$ ) on grounded ice (dark orange to blue colour scale) for each 4–5 year epoch. (d–f) Median Lagrangian  
 301 basal ~~accumulation-mass change~~ rate ( $M_b$ , negative for basal melt) for each 4–5 year epoch. All maps (a–f) overlie the most recent  
 302 annual mosaic hillshade from each epoch. (g) total Lagrangian thickness change ( $DH_E$ ) on floating ice and total Eulerian thickness  
 303 change ( $dH$ ) on grounded ice for the entire study period. (h) Median  $DH_E/Dt$  and  $dH/dt$  for the entire study period. (i) Median  $M_b$

304 for the entire study period. Maps for the entire study period (g–i) overlie the 200 m REMA mosaic. All maps show the IPY GL as  
305 a black curve, and the reference channels as green curves, and (a–f) show the most recent HB in each epoch as a blue curve.

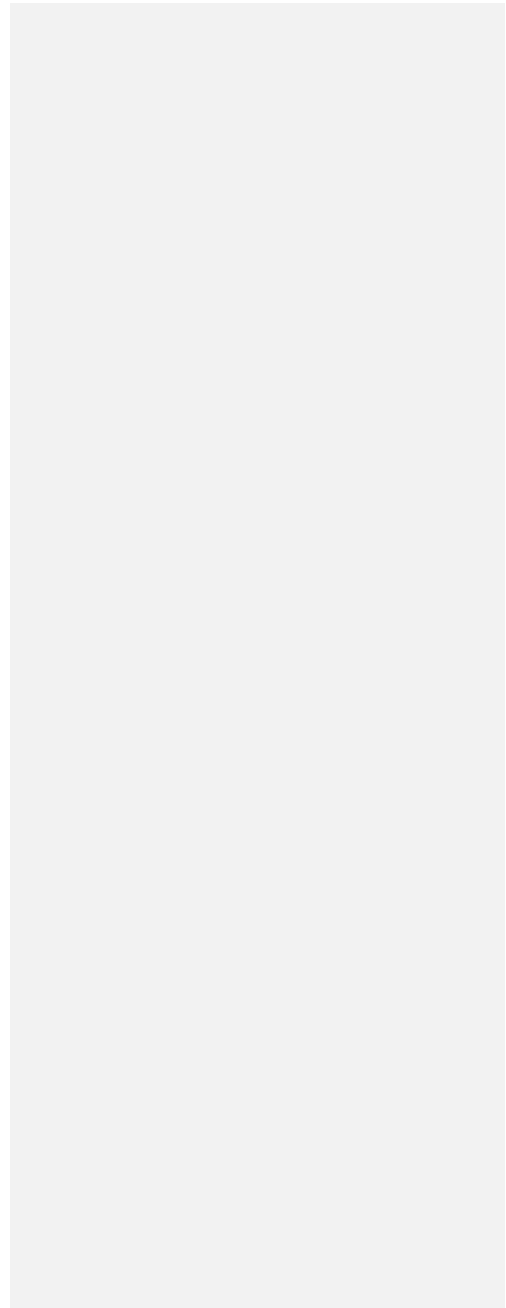
306

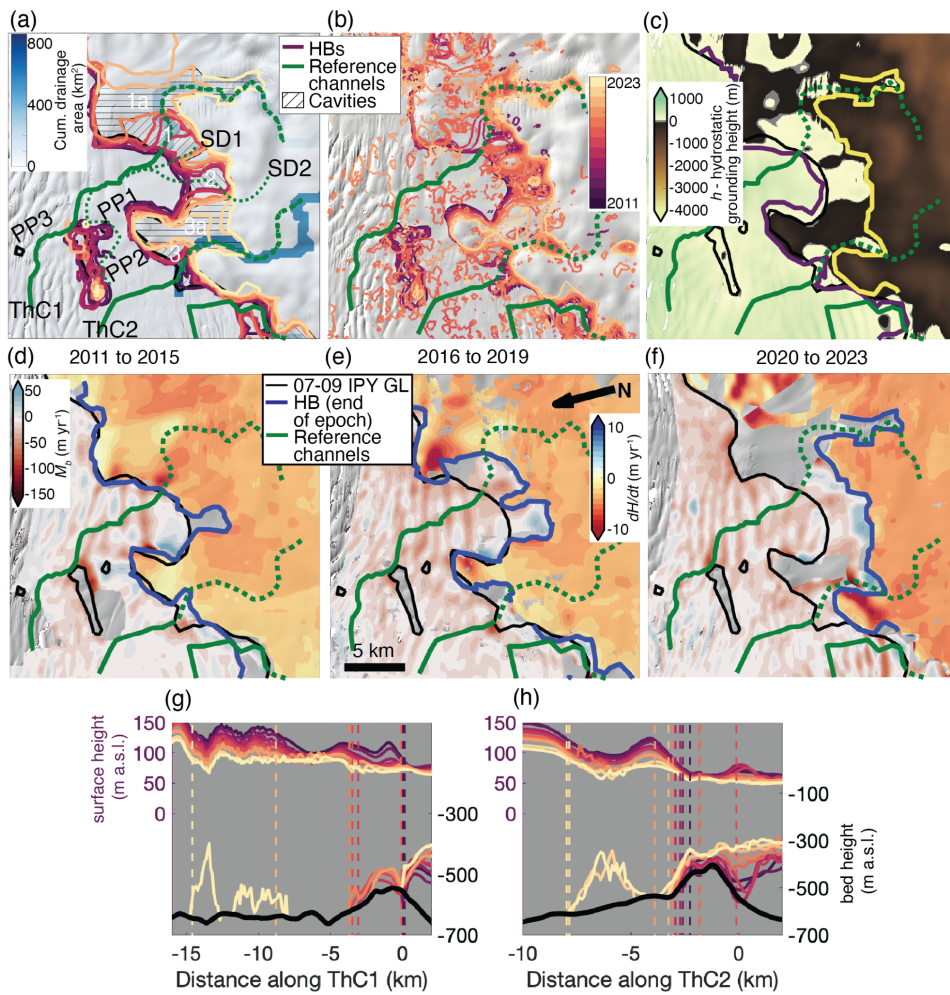
#### 307 4 Results

308 The TGIS has REMA coverage from November 2010 to December 2022, enabling investigation of time-evolving HB and  
309 ice-shelf/basal channel positions as well as ice-column thinning and basal melt rates over the entire ice shelf at unprecedented  
310 spatial resolution (Section 4.1). The HB retreated or was stagnant everywhere in the study area (Fig. 1) and ice-column  
311 thinning, and basal melting and grounded ice thinning dominated rates of change throughout the study period (Figs. 2, S7).

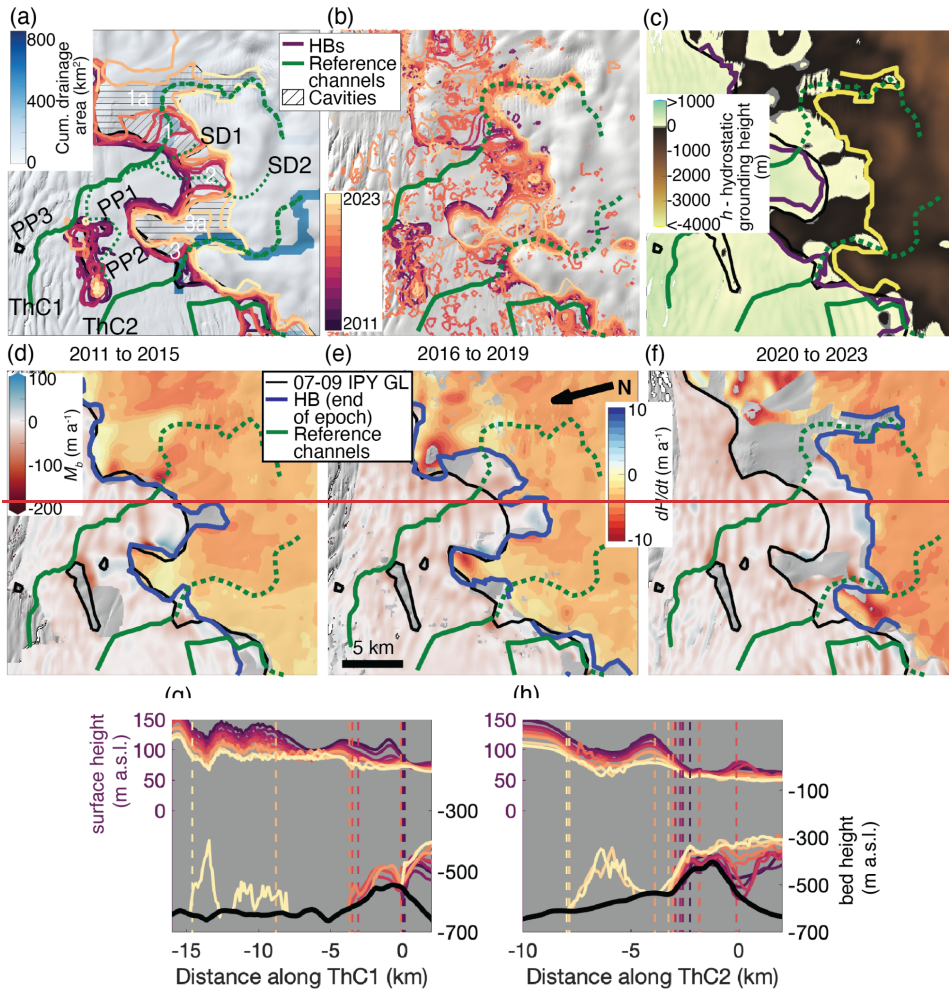
312 We identify nine regions of significant HB retreat and growth of basal cavities, labelled Cavities 1–9 (Fig. 1), discussed in  
313 more detail below (Section 4.2). Seven ice-shelf/basal channels that originate near the grounding zone/GZ are consistently  
314 identified throughout the study period, labelled ThC1–7 (Fig. 1). Six/Several of the channel locations align with inferred  
315 subglacial drainage routes (Figs. 3–5a), as discussed in more detail below (Section 4.2).

Commented [19]: R1 "Several". Why not be precise here?









319 **Figure 3:** (a–f) Zoom on Box A from Fig. 1, showing reference channels ThC1–2 (thick green solid/dashed curves) and the 07–09  
 320 IPY GL (black curve). (a) Cumulative subglacial drainage area (blue colour scale, explained in Section 3.4) with the smoothed annual  
 321 HBs (purple–orange–yellow curves, with less recent, darker features plotted below more recent features as lighter colours) and  
 322 Cavities 1–3 (hatched regions). Prominent surface depressions that are possibly connected to ThC1 are highlighted by thin dotted  
 323 green curves. (b) Unfiltered HB features for each year (also on the purple–orange–yellow colour scale used for smoothed annual

Commented [20]: R2 (g) and (h) labels are only partially visible.

324 HBs). Panels (a) and (b) use the REMA v4 200 m mosaic hillshade as the base map. (c) Difference between the 2019 surface height  
325 and the hydrostatic grounding height (which is the flotation thickness plus the BedMachine v3 bed height) overlain by the smoothed  
326 annual HBs from 2011 (purple curve) and 2023 (yellow curve). (d–f)  $M_b$  on the TGIS (dark red to blue colour scale) and  $dH/dt$  on  
327 grounded ice (dark orange to blue colour scale) for each 4–5 year epoch overlain on the most recent annual REMA mosaic hillshade  
328 from each epoch. The most recent HB in each epoch is also plotted (blue curve). Annual surface height (left axis) and ice base (right  
329 axis) and BedMachine bed height (right axis, black curve) interpolated to reference channels (g) ThC1 and (h) ThC2. Vertical dashed  
330 lines mark the most landward intersection of each year's HB with the extended channel. Distances are defined from each channel's  
331 intersection with the IPY GL, with positive distance indicating advance and negative distance indicating retreat.

#### 332 333 4.1 Time-evolving rates of basal mass change and ice thickness

334 Figures 2–5 indicate that rates of basal mass change are predominantly negative, indicating dominated by basal melting, but  
335 are spatially and temporally variable throughout the observation period, as are rates of floating ice-column and grounded ice  
336 thickness and surface-height change (Table 1). For ice shelf thickness changes in the Lagrangian frame ( $DHE/Dt$ ), thinning  
337 refers to change in the same column of ice as it advects with flow, rather than thinning at a fixed coordinate (Eulerian Frame),  
338 which we refer to on grounded ice. In general, ice-column thinning and basal melting accelerated from 2011–2015 to 2016–  
339 2019 and decelerated slightly in 2020–2023. The banded patterns of positive and negative values visible on the TEIS and  
340 TWIT in maps of  $DHE/Dt$  and  $M_b$  may be due to changes in ice velocity not accounted for in flow-shifting using annual  
341 surface-velocity maps, or due to hydrostatic compensation around growing basal crevasses (e.g. Vaughan et al., 2012).

342 Overall, the TEIS experienced less basal melting than the TWIT. Nevertheless, there was some apparent mass gain  
343 in areas of TWIT, particularly in the downstream portion of the TWIT and the shear zone between the TEIS and TWIT (Figs.  
344 2, 4–5). We expect that the apparent positive  $M_b$  in the downstream portion of the TWIT may be due to an artefact of hydrostatic  
345 disequilibrium due to transient grounding, as evidenced by the presence of isolated HB features in that region (Figs. 5b, S4b).  
346 The fastest rates of ice-column thinning and basal melting on the TEIS consistently occur at the eastern ends of pinning points  
347 PP2 and PP4, with PP2 located near a zone of rapid HB retreat (Section 4.5) and the opening of Cavity 3 (Fig. 2, Sections 4.2.1  
348 and 4.2.4, respectively).

349 The main trunk of the TWIT near the GZ experienced the most intense basal melting at rates reaching exceeding 250 m  
350  $yr^{-1}$  in places near the grounding zone GZ throughout the study period (Fig. 5). A closer look within Box B (Fig. 4d–f)  
351 shows that consistently high basal melt rates also occurred near the grounding zone GZ in the vicinity of ThC5 and Cavity 7.  
352 There is also a flow-parallel band of accelerating ice-column thinning and basal melting along ThC6 near a zone of modest  
353 HB retreat along the most pronounced inferred subglacial drainage route (Figs. 2, 5d–f, Section 4.2.3).

Commented [21]: R2 Not sure what you mean here? What other than melting would cause basal mass change? Please clarify.

Commented [22]: Ed: I 255 I supposed you mean "basal melting" (as opposed to "surface melting"). The terminology for this is not consistent throughout the paper (e.g., "ocean-induced melting" or "ocean melting" is also used elsewhere).

Commented [23]: R2 I suggest caution in how you present "thinning" over ice shelves, this is Lagrangian change in elevation – "thinning" might create confusion with the reader. I would suggest using a different term. This applies to many sections of the manuscript, where elevation and thickness change over floating ice is mentioned.

Commented [24]: Ed: I 268 Has the abbreviation TWIT been defined? Overall, there are quite a few abbreviations which might be difficult for all to follow.

Commented [25]: R1 "TEIS" and "TWIT". I would say these have gained enough currency for general adoption. But then I would.

Commented [26]: R2 Meaning that apparent refreezing is an artefact of the floating assumption? Or does the transient grounding leads to real refreezing somehow? Please clarify.

355 Table 1. Rates of change in each annual mosaic epoch. All values are in units  $\text{m yr}^{-1}\text{a}^{-1}$  (ice equivalent).

	Rate of surface height change		Rate of thickness change				Rate of basal mass change	
	Floating $Dh/Dt$		Grounded $dH/dt$		Floating $DH_E/Dt$		Floating $M_b$	
	Mean $\pm \sigma$	median	Mean $\pm \sigma$	median	Mean $\pm \sigma$	median	Mean $\pm \sigma$	median
Overall	$-0.7 \pm 4.9$	$-0.9$	$-2.2 \pm 0.7$	$-2.1$	$-14.2 \pm 27.7$	$-8.6$	$-6.2 \pm 27.9$	$-3.1$
2011–2015	$-1.0 \pm 6.3$	$-0.8$	$-2.8 \pm 1.6$	$-2.6$	$-21.4 \pm 36.9$	$-11.0$	$-14.5 \pm 37.4$	$-6.2$
2016–2019	$-3.0 \pm 5.0$	$-2.0$	$-2.4 \pm 2.2$	$-2.3$	$-27.3 \pm 35.6$	$-17.8$	$-19.0 \pm 37.6$	$-11.1$
2020–2023	$-2.7 \pm 5.1$	$-1.8$	$-2.0 \pm 2.0$	$-1.9$	$-26.2 \pm 35.3$	$-16.2$	$-16.8 \pm 34.8$	$-9.2$

356

#### 357 4.2 ~~Ice-shelf~~Basal channel–HB interactions

358 As mentioned above, the HB retreated or stagnated ~~relative to its early position~~the IPY GL everywhere by 2023, including  
 359 on pinning points, with significant variability in the rates of retreat, including some small and temporary areas of advance. In  
 360 Cavities 6–9, early HBs appear seaward of the 07–09 IPY GL, likely due to the differences in mapping method, but by 2023  
 361 the HB had also retreated or stagnated relative to the IPY GL everywhere. While few consistent spatiotemporal patterns in HB  
 362 retreat emerged, there were no areas of sustained HB advance.

363 We identify several persistent basal incisions and surface depressions along seven ~~ice-shelf~~basal channels. We reduce  
 364 the impact of noise in individual DSM strips on mapped basal incisions and surface depressions (Fig. S4) by defining fixed  
 365 reference locations of seven ~~ice-shelf~~basal channels, called ThC1–7, shown as green curves in figures, to be where the greatest  
 366 overlap of these features occurs. The reference channels are extended above the ~~grounding zone~~GZ along surface depressions  
 367 (where present) on grounded ice, shown as thick-dotted green curves in figures, enabling us to measure changes in surface  
 368 height (Figs. 2–5g–i), thickness (Fig. 6b) and velocity (Figs. 6 and 7) along the reference channels, as well as changes in their  
 369 intersections with the HB from each year relative to their intersections with the 07–09 IPY GL (Figs. 3–6), referred to as the  
 370 ThCX–IPY GL intersection. IceBridge MCoRDS ~~IPR~~ice–thickness profiles were queried to verify the presence of the  
 371 ~~seven~~eight ~~ice-shelf~~basal channels identified, although data quality along some profiles is poor (Figs. S4–5). There are also

Commented [27]: R2 Is it “everywhere”? In several sectors (cavities 6, 7, 8 & 9), IPY GL appear to be inland of the HB position in ~ 2011 and 2012. Given the importance of this sector it is probably worth discussing and providing potential explanation for this.

Commented [28]: R1 seven, then eight basal channels?



372 several persistent surface depressions that extend inlandupstream of the IPY GL but do not appear aligned with mapped ice-  
373 shelfbasal channels, labelled SD1–7 and marked by thin dotted green curves in (Fig. ures 3a, and 5a).

374 A variety of behaviours and interactions between the ice-shelfbasal channels and the grounding zoneGZ are observed.

375 We distil these into three major types:

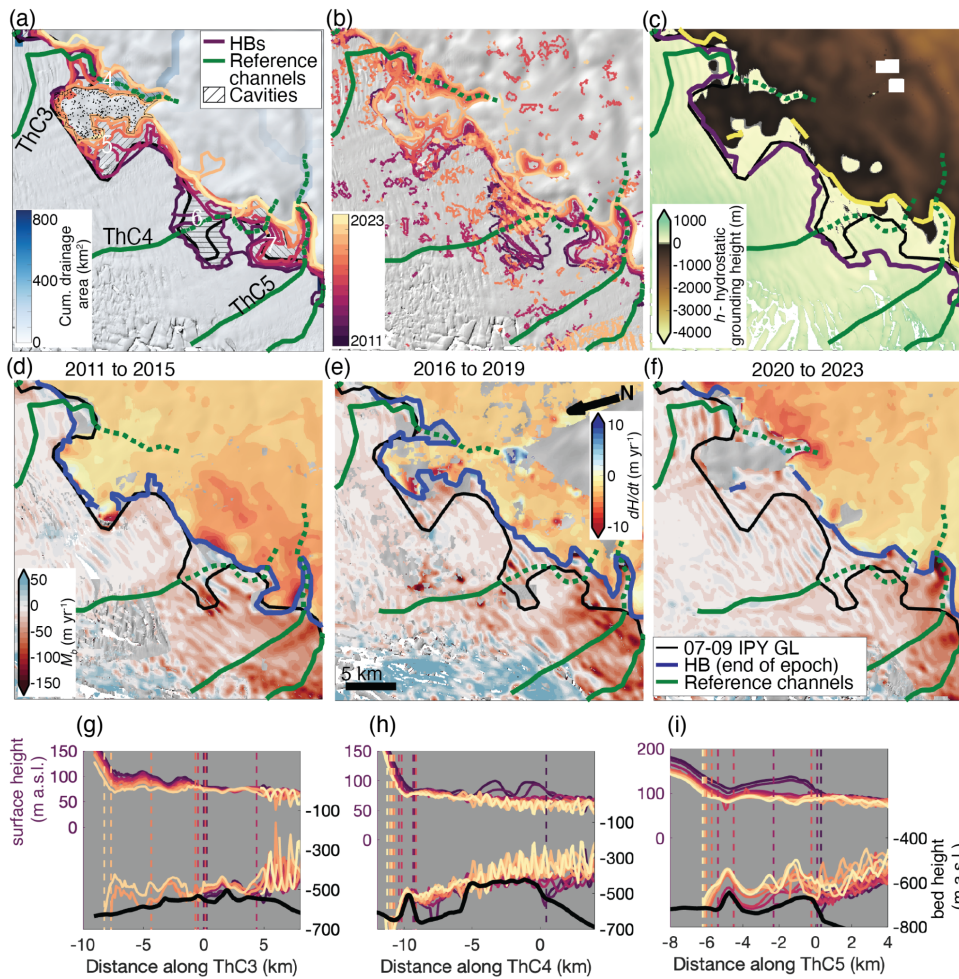
- 376 1. Narrow-cavity HB retreat along a narrow band parallel to an ice-shelfbasal channel (ThC2, ThC3, ThC5; Section  
377 4.2.1)
- 378 2. Wide-cavity retreat along an ice-shelfbasal channel (ThC1, ThC4; Section 4.2.2)
- 379 3. Little to no HB retreat at the inland-upstream ends of ice-shelfbasal channels (ThC6, ThC7; Section 4.2.3).

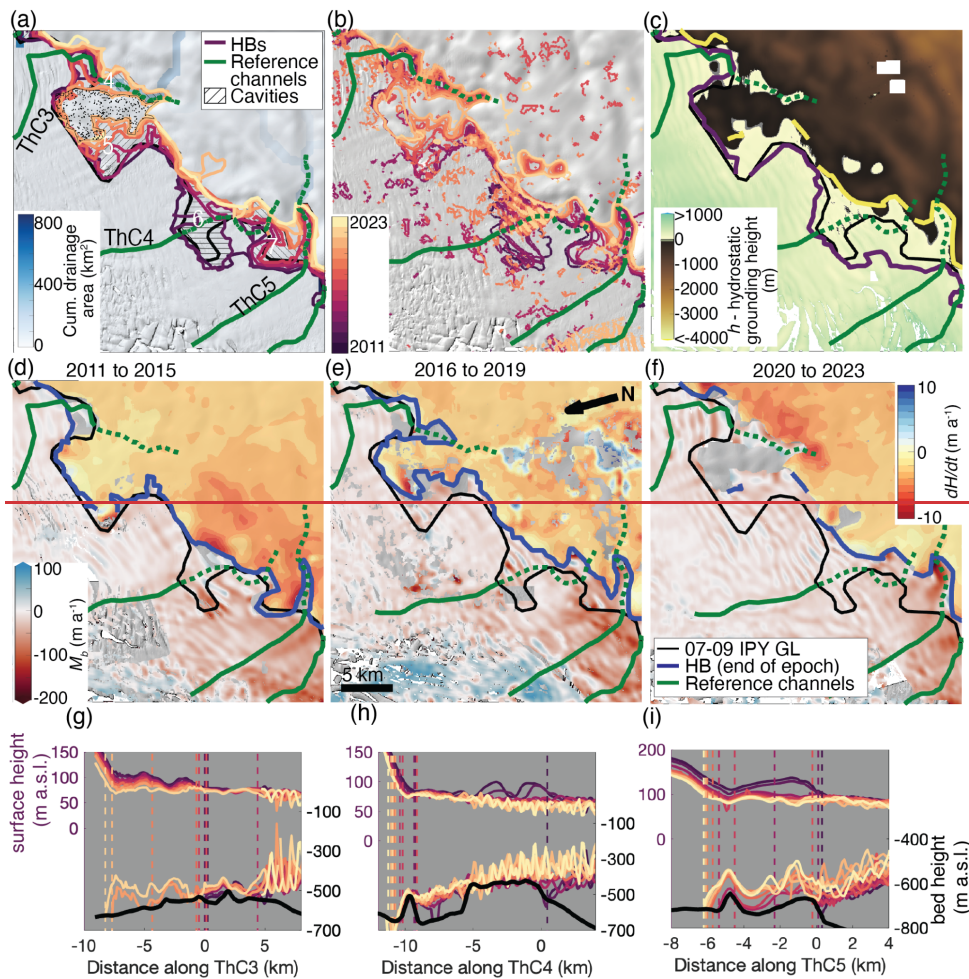
380 Figure 6a shows a time series of the change in position of the HB's intersection along each reference channel and illustrates  
381 that Type 1 retreat tended to involve more steady retreat and Type 2 retreat tended to involve cycles of rapid retreat followed  
382 by stabilisation. It is important to note that we do not consider these types to be mutually exclusive, as more than one type of  
383 HB retreat is observed along several ice-shelfbasal channels throughout the study period.

384 Several TGIS-wide similarities among ice-shelfbasal channels are observed. The grounded ice within ~5 km of each  
385 channel's inlandupstream end had background thinning rates between  $-1$  to  $-4$  m  $\text{yr}^{-1}$  (Figs. 2a–c, 3–5d–f). All channels  
386 except for ThC4 originate near areas of high cumulative subglacial drainage area at the grounding zoneGZ (Figs. 3–5a). Retreat  
387 of the HB exceeding 1 km occurred along all reference channels except for ThC6 and ice-column thinning and basal melting  
388 occurred near all channel intersections with the grounding zoneGZ within at least one multi-year epoch by the end of the study  
389 period (Figs. 2–6). Notably, the mean velocity along each HB is slightly slower at the ThCX–HB intersections than in non-  
390 channelized portions of the grounding zoneGZ (Fig. 6c). However, no strong relationships emerge between changes in velocity  
391 and HB retreat rates along all channels each channel; notable correlations between changes in velocity and changes in HB  
392 position along individual channels are described in ensuing sections (Fig. 7).

Commented [29]: R1 "by the end of the study period".  
You could help the reader here by giving precise time  
boundaries.

Commented [30]: R1 I couldn't see how Figure 7 could  
be used as evidence here.





396 Figure 4: (a–f) Zoom on Box B from Fig. 1, showing reference channels ThC3–5 (thick green solid/dashed curves) and the 07–09 IPY  
 397 GL (black curve). (a) Cumulative subglacial drainage area (blue colour scale) with the smoothed annual HBs (purple–orange–  
 398 yellow curves, with less recent, darker features plotted below more recent features as lighter colours) and Cavities 4–7 (hatched  
 399 regions). (b) Unfiltered HB features for each year (also on the purple–orange–yellow colour scale used for smoothed annual HBs).  
 400 Panels (a) and (b) overlie the REMA 200 m mosaic hillshade. (c) Difference between the 2019 surface height and the hydrostatic  
 23

401 grounding height overlain by the smoothed annual HBs from 2011 (purple curve) and 2023 (yellow curve). (d–f) Mb on the TGIS  
402 (dark red to blue colour scale) and  $dH/dt$  on grounded ice (dark orange to blue colour scale) for each 4–5 year epoch overlain on the  
403 most recent annual REMA mosaic hillshade from each epoch. The most recent HB in each epoch is also plotted (blue curve). Annual  
404 surface height (left axis) and ice base (right axis) and BedMachine bed height (right axis, black curve) interpolated to reference  
405 channels (g) ThC3, (h) ThC4, and (i) ThC5. Vertical dashed lines mark the most landward intersection of each year's HB with the  
406 extended channel. Distances are defined from each channel's intersection with the IPY GL, with positive distance indicating advance  
407 and negative distance indicating retreat.

#### 409 4.2.1 Type 1: Sustained retreat along narrow cavities

410 Channels ThC2, ThC3, and ThC5, as well as ThC1 in more recent years, were associated with steady, sustained HB retreat  
411 along narrow cavities. These features are each directly aligned with an inferred subglacial drainage pathway (Figs. 3–5a) along  
412 which HB retreat occurred, such that the cavities may strike oblique to the flow direction, but parallel to the surface depressions.  
413 Furthermore, the profiles for these reference channels show large undulations in bed and surface height within 5–10 km of  
414 their intersections with the IPY GL grounding-line (Figs. 3–4g–i) which make it difficult to interpret  $DH/Dt$  and  $M_b$  in these  
415 cavities because the flow—shifting does not fully account for height changes due to horizontal advection, leading to alternating  
416 bands of apparent ice-column thinning/basal melting and thickening/basal mass gain near the grounding zoneGZ (Figs. 3–4d–  
417 f).

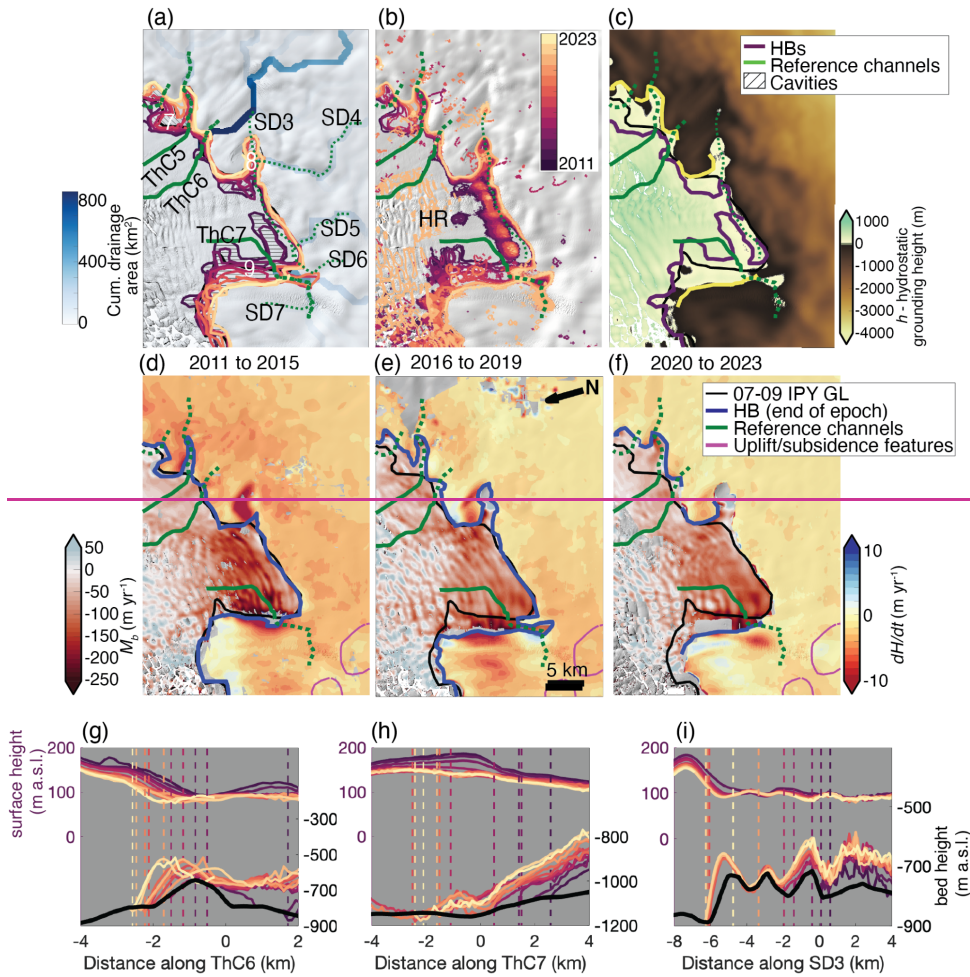
418 The HB intersection with ThC2 predominantly exhibited Type 1 retreat as the HB retreated in a narrow band along  
419 the sinuous ThC2 and its inferred underlying subglacial drainage route throughout the study period (Fig. 3). Cavity 3 widened  
420 suddenly following a few years of retreat in a narrow band, temporarily exhibiting Type 2 characteristics, before growing  
421 further inlandupstream in a narrow band. Between 2021–2023, continued HB retreat opened all of Cavity 3a so that it merged  
422 with Cavity 2 (Fig. 3a), coinciding with a 20% increase in surface velocity along ThC2 after relatively steady speeds in earlier  
423 years (Fig. 7). Figures 5c and 5h show that Cavity 3a overlies a bedrock ridge, and that the inlandupstream end of ThC2  
424 overlies a deepening trough. Rapid ice-column thinning and basal melt occurred near the intersection between ThC2 and the  
425 grounding zoneGZ throughout the study period (Figs 2, 3d–f).

426 The HB position change along ThC3 exhibits the clearest example of Type 1 retreat (Figs. 1, 4). Figures 4a–b and 4g  
427 show that the HB remained relatively stationary relative to ThC3 on a small bedrock ridge through 2018, before retreating  
428 rapidly along ThC3 down a retrograde bed slope at a rate of 3.5 km  $\text{ayr}^{-1}$  between 2018–2020, opening the narrow Cavity 4  
429 (Fig. 3a). HB retreat slowed in subsequent years despite the retrograde bed slope continuing inlandupstream. Despite the  
430 banded pattern in the Mb melt-rate maps in this region, it appears that basal melt rates generally intensified throughout the  
431 study period (Figs. 4d–f). As observed along ThC2, surface velocity along ThC3 accelerated between 2020–2023, although  
432 retreat had slowed by this time (Fig. 7).

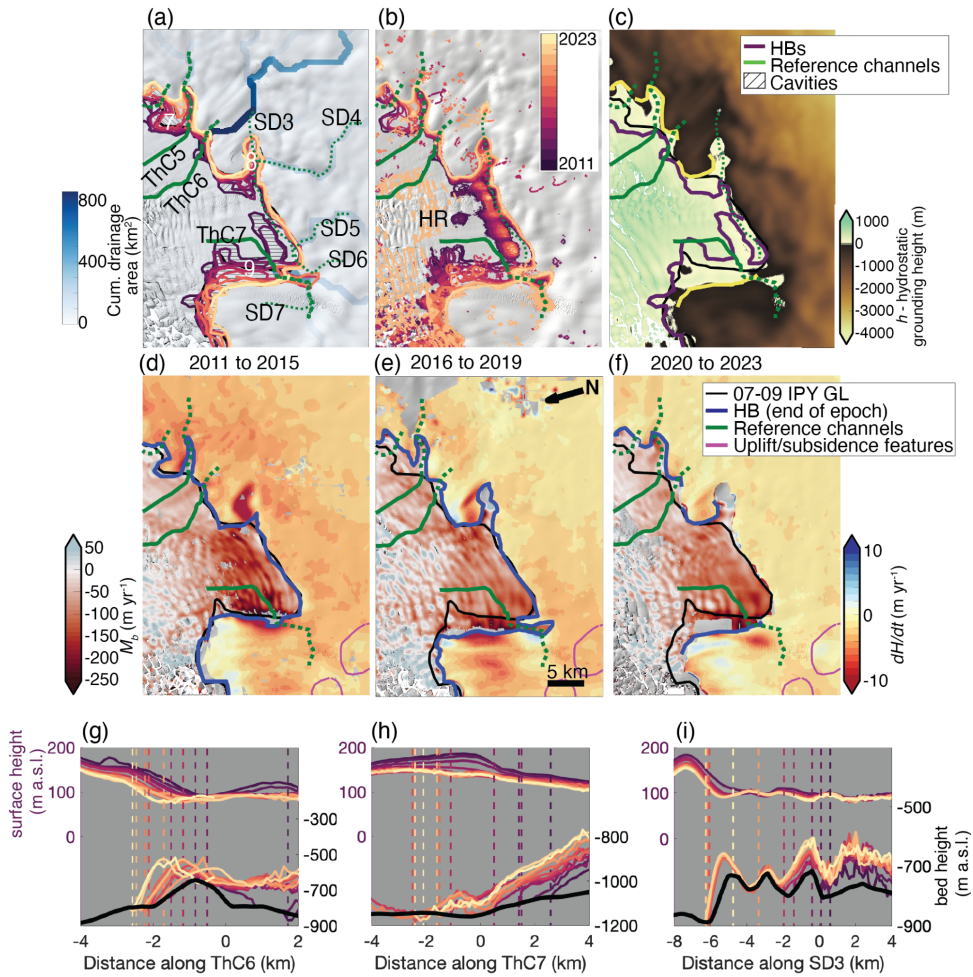
433 Figure 4 shows that the HB retreated south—eastward along ThC5 at an average rate of  $\sim 0.7$  km  $\text{yr}^{-1}\text{a}^{\pm}$  between  
434 2013–2018, forming the finger—like southern portion of Cavity 7. During this time, ice-column thinning and basal melt rates  
435 reached 100 m  $\text{yr}^{-1}\text{a}^{\pm}$  and 60 m  $\text{yr}^{-1}\text{a}^{\pm}$ , respectively, (Figs. 4d–e) along ThC5 as the HB breached successive bedrock ridges

436 before stagnating on a relatively flat bed about 5–7 km ~~up~~<sup>up</sup> ~~glacier inland~~ of the ThC5–IPY GL intersection (Fig. 4i). Although  
437 the HB didn't retreat much further along ThC5, Cavity 7 widened eastward and merged with Cavity 6. During this time, basal  
438 melt rates within Cavity 7 intensified, exceeding 100 m ~~yr~~<sup>yr</sup> ~~la~~<sup>la</sup> along ~~the~~ ThC5 (Fig. 4f).

439







441  
 442 **Figure 5:** (a–f) Zoom on Box C from Fig. 1, showing reference channels ThC6–7 (thick green solid/dashed curves) and the 07–09  
 443 IPY GL (black curve). (a) Cumulative subglacial drainage area (blue colour scale) with the smoothed annual HBs (purple–orange–  
 444 yellow curves, with less recent, darker features plotted below more recent features as lighter colours) and Cavities 7–9 (hatched  
 445 regions). Prominent surface depressions SD3–7, some of which are possibly connected to ThC7, are highlighted by thin dotted green  
 446 curves. (b) Unfiltered HB features for each year (also on the purple–orange–yellow colour scale used for smoothed annual HBs).

447 with an HB in the TWIT labelled “HR” for the “Holland Rumples” that was mapped by Holland et al., (2023). Panels (a) and (b)  
448 overlie the REMA 200 m mosaic hillshade. (c) Difference between the 2019 surface height and the hydrostatic grounding height  
449 overlain by the smoothed annual HBs from 2011 (purple curve) and 2023 (yellow curve). (d–f)  $M_b$  on the TGIS (dark red to blue  
450 colour scale) and  $dH/dt$  on grounded ice (dark orange to blue colour scale) for each 4–5 year epoch overlain on the most recent  
451 annual REMA mosaic hillshade from each epoch. The most recent HB in each epoch is also plotted (blue curve) and uplift/subsidence  
452 features identified by Rignot et al. (2024) (magenta curves). Annual surface height (left axis) and ice base (right axis) and  
453 BedMachine bed height (right axis, black curve) interpolated to reference channels (g) ThC6, (h) ThC6, and (i) SD3. Vertical dashed  
454 lines mark the most landward intersection of each year’s HB with the extended channel. Distances are defined from each channel’s  
455 intersection with the IPY GL, with positive distance indicating advance and negative distance indicating retreat.

#### 457 4.2.2 Type 2: Wide-cavity retreat

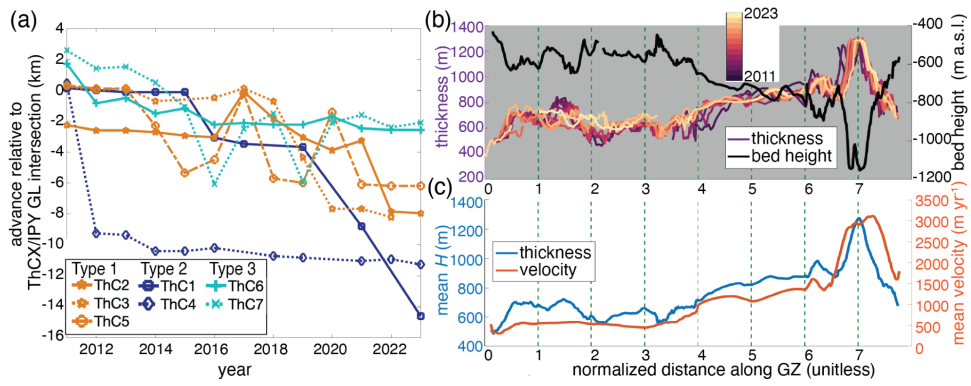
458 Channels ThC1 and ThC4 are associated with sudden, rapid HB retreat off of bedrock highs to form wide Cavities 1a, 2, and  
459 6, respectively (Figs. 3–4). Expansion of these relatively large cavities mostly occurred during 2013–2016 as widening across-  
460 flow.

461 ThC1 and merging surface depressions SD1 and SD2 intersect the IPY GL in a region where the TEIS cavity is deeply  
462 embayed. Figure 3a shows that Cavity 1 opened up as the HB retreated suddenly along the ThC1 surface depression and an  
463 inferred subglacial channel between 2015 and 2016, and that Cavity 2 opened up as the HB retreated suddenly along SD2  
464 (which does not align with an inferred subglacial channel) between 2014 and 2015, forming the lobes that make this region  
465 known as the “butterfly” region. At the same time, the velocity along ThC1 accelerated after a period of stability between  
466 2011–2015 and continued to accelerate throughout the study period (Fig. 7). As basal melt rates accelerated to near 40 m  $\text{yr}^{-1}$   
467  $\text{a}^{-1}$  by 2016–2019 (Fig. 3e), Cavities 1 and 2 widened but did not extend further inlandupstream (Fig. 3a). Cavity 2 merged  
468 with Cavity 1 between 2021–2022, eliminating the butterfly shape that was prominent in earlier years. After 2019, the HB  
469 exhibited Type 1 retreat, as the narrower Cavity 1a extended inlandupstream along the ThC1 surface depression and underlying  
470 inferred subglacial channel at a rate exceeding 2 km  $\text{yr}^{-1}$   $\text{a}^{-1}$  (Figs 3, 6a).

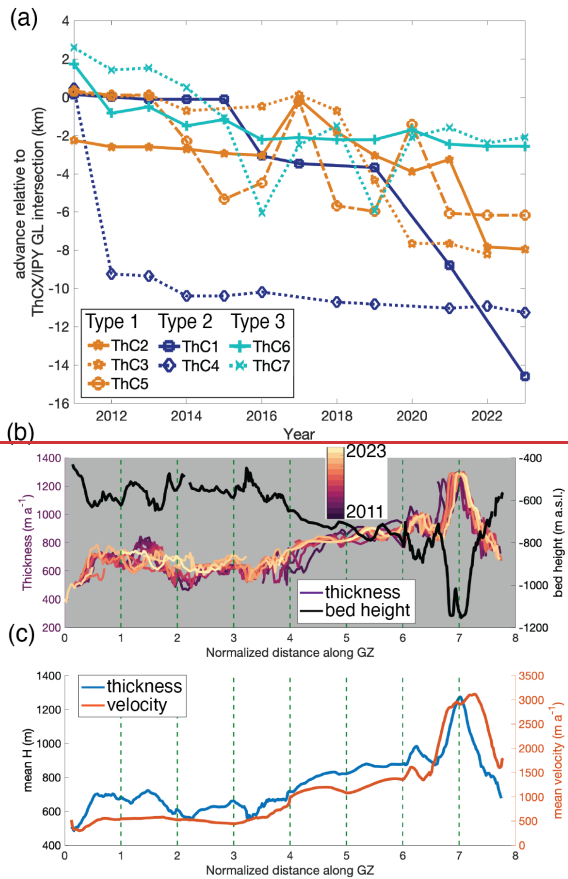
471 ThC4 is situated near the western edge of the TEIS and does not align with an inferred subglacial hydrological route.  
472 ThC4 appears to result from the merging of two incisions initiated at two bedrock ridges, the wider of which is located at  $\sim$ 5  
473 to 0 km along ThC4 in Figures 4h and 7 (where 0 km is the northernmost ThC4–IPY GL intersection); the narrower ridge is  
474 located further south at about  $\sim$ 9.2 km in Figures 4h and 7, near the western end of Cavity 7 (Fig. 4a). Several instances of  
475 the sinuous surface depression persist across Cavities 6 and 7 (Fig. S4c), while instances of the basal incision appear to curve  
476 around Cavity 6 (Fig. S4a). Figure 4h shows that Cavity 6 opened along ThC4 between 2011–2015 as ice ungrounded from  
477 the wide ridge. In subsequent years, Cavity 7 reached its eastern and southern maximum extents and merged with Cavity 6 as  
478 the HB retreated off the narrower southern bedrock ridge (Figs. 4a, 4h). Despite basal melt rates consistently exceeding 60 m  
479  $\text{yr}^{-1}$   $\text{a}^{-1}$  near ThC4 (Fig 4d–f, which may be unreliable due to possible intermittent re-grounding, indicated by the isolated  
480 HBs in Figure 4b), the HB did not retreat much further along ThC4, stabilising within a bedrock trough (Fig. 4h). The velocity  
481 along ThC4 was highly variable, decelerating by about 5% as Cavity 6 grew, accelerating by about 10% between 2015–2016,



482 slowing again between 2016–2019 as Cavity 7 grew, and speeding up, especially downstream of Cavity 6, as the HB stagnated  
483 (Fig. 7).  
484



485



486  
 487 **Figure 6: (a) Time series of HB position along each reference channel, with negative distance indicating retreat, and 0 km marking**  
 488 **the ThCX/IPY GL intersection. The orange time series indicate Type 1 retreat, the blue time series indicate Type 2 retreat, and the**  
 489 **teal time series indicate Type 3 retreat. (b) Thickness along each annual HB and BedMachine bed height along the IPY GL and (c)**  
 490 **mean thickness and velocity along the IPY GL, with unitless distance normalised to the intersection of each year's HB or the IPY**  
 491 **GL with each ice-shelf channel ThC1-7. Annual thickness and (c) mean thickness and velocity along the HB, with unitless distance**  
 492 **normalised to the intersection of each year's HB with each ice-shelf basal channel ThC1-7.**

493

494 **4.2.3 Type 3: Little to no HB retreat**

495 ~~Ice-shelf~~Basal channels ThC6 and ThC7 were associated with modest HB retreat that did not fit into Type 1 or Type 2 cavity  
496 shapes, despite their alignment with inferred subglacial drainage routes (Fig. 5).

497 ThC6 is aligned with the strongest inferred subglacial channel just east of the TWIT ~~main trunk~~GZ ~~embayment~~, but  
498 the surface depression does not appear to extend ~~inland~~~~upstream~~ of the IPY GL (Figs. 4a, S4c). Thus, ~~we manually extended~~  
499 ~~the~~~~the~~ ~~landward~~~~upstream~~ end of the ThC6 reference channel ~~was extended about 5 km inland of~~past the ~~grounding zone~~GZ  
500 ~~to show retreat past the IPY GL~~arbitrarily. Throughout the study period, rapid ~~thinning and~~basal melt ~~and grounded and~~  
501 ~~floating ice thinning~~ occurred near the ThC6–IPY GL intersection (Fig. 5d–g). The HB retreated at a rate of about 0.3 km ~~yr~~  
502 ~~1a~~<sup>+</sup> along ThC6 (Fig. 6a), and the small cavity forms a ~~v~~–shape along the inferred subglacial channel (Fig. 5a), potentially  
503 indicating that Type 2 retreat will occur in the future. ThC6 also experienced among the widest fluctuations in velocity,  
504 although there was no clear relationship between velocity and HB retreat ~~or rates of thinning~~ (Fig. 7).

505 The western ~~flank~~ GZ of the TWIT ~~main trunk grounding zone~~GZ ~~embayment~~ exhibits complex morphology and  
506 changes, but relatively slow rates of retreat in the vicinity of ThC7 and merging surface depressions SD6–7 (Fig. 5a). At ThC7,  
507 the HB retreated ~0.4 km ~~yr~~–1~~a~~<sup>+</sup> as Cavity 9 extended westward between 2013–2023 (Fig. 6a), ~~with basal~~consistently ~~thinning~~  
508 ~~and melting at~~ rates ~~consistently~~ exceeding 100 m ~~yr~~–1~~a~~<sup>+</sup> (Figs. 5, 6a). Notably, in 2016 and 2019, the HB temporarily retreated  
509 along a narrow band along the ThC7 surface depression (Fig. 5i), within the same timeframe as a 300 m ~~yr~~–1~~a~~<sup>+</sup>, or 11%,  
510 increase in velocity between 2016–2020 (Fig. 7).

511

Commented [31]: R1 "was extended .. arbitrarily".  
Please explain more precisely what you mean.

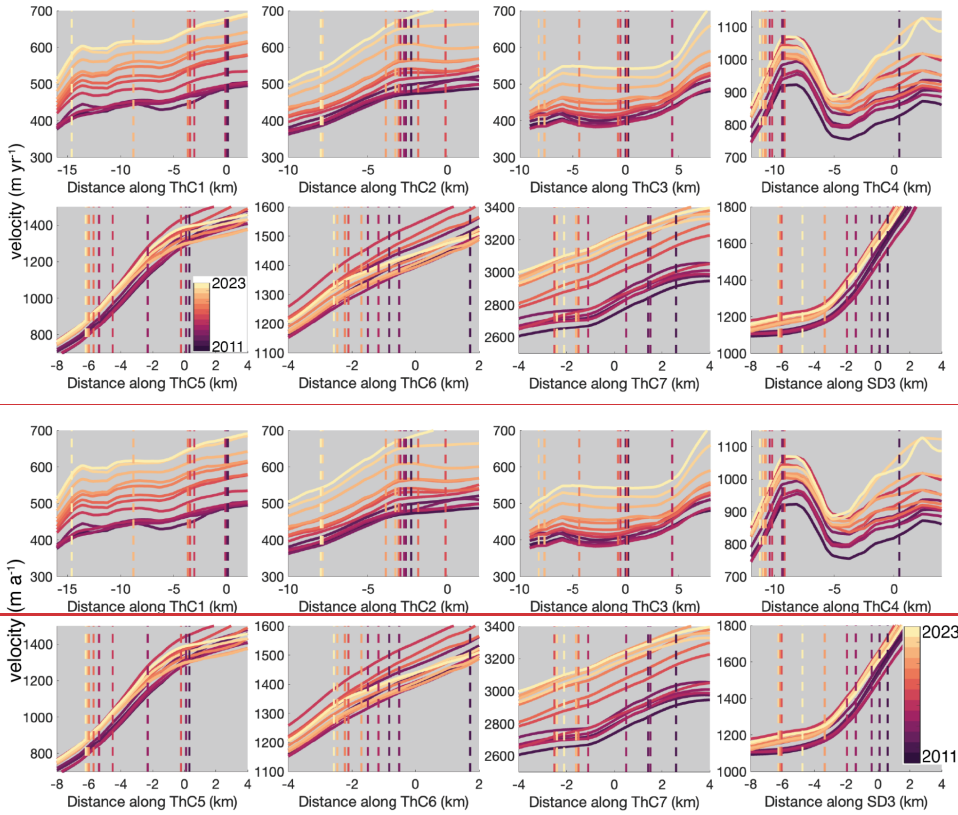


Figure 7: MEaSUREs annual velocity (2011–2015) and averaged summer quarterly velocities from InSAR (2016–2023) interpolated to reference channels ThC1–7 and SD3. Vertical dashed lines mark the most landward intersection of each year's HB with the reference channel. Distances are defined from each channel's intersection with the IPY GL, with positive distance indicating advance and negative distance indicating retreat.

#### 4.2.3 Retreat not associated with ice-shelf basal channels

There are a few regions where HB retreat is observed in the absence of ice-shelf basal channels and/or inferred subglacial drainage routes. Between ThC3 and ThC4, there is a region where the HB shifts eastward between 2013 and 2021 at a rate of

522 up to 0.6 km  $\text{yr}^{-1}\text{a}^{-1}$ , opening Cavity 5 (Fig. 4). Notably, the 2022 HB connects with Cavity 4, indicating that a larger cavity  
523 may have opened, but there was insufficient coverage to map the 2023 HB in this region (stippled area in Fig. 4a). Since the  
524 2022, this region only has coverage from one or two strips (Fig. S2), resulting in only two mappings of HB features from  
525 which the annual HB was manually delineated. Although some regions are covered by few strips in several years, we are more  
526 confident in HB positions that persist or display a pattern over several years, and one year of data does not provide sufficient  
527 evidence to conclude that this may be a bias in the surface height in this region which impacts the HB position, could have  
528 resulted from the coverage of an individual strip, or an error in the manual delineation of the annual HB, we do not consider  
529 that entire region waste to be ungrounded in 2022.

530 The main trunk of the TWIT exhibited complex HB changes seemingly independent of ThC7. Merging surface  
531 depressions SD3 and SD4 are identified inlandupstream of the south-eastern corner of the embayed grounding zoneGZ in the  
532 main trunk of the TWIT and appear to be associated with HB retreat (Fig. 5a, S4c). SD4 aligns with an inferred subglacial  
533 channel, but SD3 does not (Fig. 5a). We also identify a surface depression extending from SD3 and SD4 parallel to the IPY  
534 GL at the southern grounding zoneGZ of the main trunkboundary of the TWIT, but IPR transects M6 and M7 do not indicate  
535 that there are corresponding basal incisions (Fig. S5). The surface depression extending across the main trunkTWIT may  
536 instead be a dynamical response to the transition of flow off the ridge along the southern grounding zoneGZboundary of the  
537 main trunkGZ-embayment (Fig. S8a). Figures 5 and 6a show that the HB retreated along SD3 at an average rate of  $\sim 0.8$  km  
538  $\text{yr}^{-1}\text{a}^{-1}$  between 2011–2018, opening the narrow Cavity 8 along an undulating bedrock topography. The fastest retreat rates  
539 ( $\sim 2$  km  $\text{yr}^{-1}\text{a}^{-1}$ ) occurred between 2015–2017, followed by relative stability over a bathymetric low after 2018. Ice-column  
540 thinning and Mbasal melt rates and thinning rates were consistently high at the downstream end of Cavity 8, exceeding 100 m  
541  $\text{yr}^{-1}\text{a}^{-1}$  along the eastern flank of the main trunkIPY-GL in all three multiyear epochs (Figs. 2, 5d–f).

542 Figure 5b shows that the TWIT main trunk contained many small, isolated HBs throughout most of the study period  
543 that may indicate intermittent grounding, although the bed height is unreliable here due to the use of indirect measurements  
544 for bed heights in ice-shelf cavities (Fig. S8, (Morlighem et al., 2020)). The annual HBs from the early years of the study  
545 period extended eastward in a narrow band between ThC7 and the IPY GL, narrowing the ice-shelf cavity in the centre of the  
546 main trunkTWIT to only 2.5 km (Figs. 5a–b). By 2013, Cavity 9 had opened and the HB was approximately at the same  
547 location as the IPY GL along the southern grounding zoneGZmargin of the main trunkTWIT-embayment. Furthermore, the  
548 HB at the western flankedge of the TWIT-GZ-embayment retreated steadily to the west and up a ridgeslope in the basal  
549 topography throughout the study period (Figs. 5a, S8a). The western flank of the main trunkedge of the embayment also  
550 experienced high rates of ice-column thinning and basal melting throughout the study period as Cavity 9 opened (Figs. 2, 5d–  
551 f).

Commented [32]: R1 "or an error in the manual delineation". This alerted me to the fact that I had missed that a manual step is involved in the method - I had assumed that the process was automated. Perhaps you could expand the methods section to explain this in a nit more detail and discuss the potential errors. Errors in manual steps are rather different from uncertainties in automated processing. I think this sentence needs some more nuance.

Commented [33]: R1 extra brackets.

552 **4.3 Pinning points**

553 The HBs at the pinning points exhibited a variety of behaviours. Our HBs maps did not capture PP3, although PP1, PP2, and  
554 PP4–6 were mapped. The IPY GL did not contain a pinning point in the main trunk of the TWIT, although Holland et al.  
555 (2023) track the evolution of an ice rumple near the centre of the main trunk, which disappeared between 2011–2022. We only  
556 map PP1 through 2014, and PP2 grew smaller through 2023 (Fig. 3). Pinning points 1 and 2 experienced relatively high rates  
557 of ice-column thinning and basal melting at the eastern extent of the IPY GL of PP2 (Figs. 2, 3d–f). Furthermore, ThC1  
558 possibly rerouted as these pinning points shrank; from 2011–2014, the surface and basal manifestations of ThC1 curved toward  
559 the west, following the western prong of the “y” shape south of PP1, then straightened toward the eastern prong of the “y”  
560 shape between 2015–2022 (Fig S4).

561 Pinning points 4 and 5 were mapped throughout the study period, without much change in HB position, and the  
562 surrounding ice shelf experienced ice-column thinning and basal melting at rates similar to the rest of the TEIS (Figs. 1–2).  
563 We observe possible north–westward growth of PP4 and PP5 but note that BedMachine is poorly constrained here (Fig. S8).  
564 Pinning point 6 was also mapped throughout the study period, although it is largely indistinguishable from other small, noisy  
565 HBs that are mapped, but filtered out, on the bedrock high in the TWIT that region (Figs. 1, S4d).

566 As discussed in Section 4.2.3, the unfiltered HBs in the TWIT (Fig. 5b) indicate the presence of many small pinning  
567 points, which appear to shrink or disappear over time as the ice thins. We also map an isolated HB near the ice rumple mapped  
568 by Holland et al. (2023; labelled “HR” for “Holland Rumples” in Figure 5b) which disappears by 2014. However, as noted  
569 elsewhere, the bed topography is poorly constrained in this cavity so the locations of HBs and basal incisions inferred using  
570 the hydrostatic assumption are uncertain. Notably, the TWIT lost an area of ~1270 km<sup>2</sup> between 2011–2012, retreating from  
571 potential pinning points near the front, and continued to lose area throughout the study period (Fig. S2).

572 **5 Discussion**

573 This work reveals high-resolution observations of important processes affecting the shape and structure of the Thwaites  
574 Glacier and TGIS. We observe evidence for high rates of grounding zone retreat along ice-shelf-basal channels and  
575 inland upstream subglacial channels on the Thwaites Glacier and TGIS using REMA DSMs to map ice-shelf-basal channels,  
576 surface depressions, and rates of thickness and basal mass change. We observe three major types of retreat along seven ice-  
577 shelf-basal channels and associated surface depressions: narrow-cavity retreat, wide-cavity retreat, and little to no retreat.  
578 Regions associated with each type of retreat are often collocated with high rates of ice-shelf basal mass loss and ice-column  
579 thinning both up- and down-stream of the grounding zone and grounded ice thinning inland, particularly in the 2011–  
580 2015 epoch (Fig. 2).

Commented [34]: R2 I am curious whether you observe the pinning point evolution at TWIT described in: <https://doi.org/10.1029/2023GL103088> from the unfiltered figure 5 it appears so but it would be worth a mention, and why this pinning point may or may not be more robust than the other unfiltered HB features.

Commented [35]: Both reviewers:  
R1: It is understandable that the (very) recent paper by Eric Rignot (Widespread seawater intrusions...) is not mentioned in this study, probably because it was in review as this paper was being submitted. I recommend that the authors include this paper in their review not simply because it is relevant, but because it could serve to clarify the relationship between the transition zone between grounded and floating ice as detected by InSAR and the Hydrostatic Boundary as measured by DSM analysis. Professor Rignot's paper finds evidence of seawater-induced vertical motion inland beyond the HBs in this paper and the discussion could be quite informative. The adoption of informal names of some sub-glacial features may also be appropriate. From the present high quality of argumentation and discussion I doubt it will take long to add this potentially valuable element.

R2 It would be good for the discussion to reflect on the implication of the findings in light of the recent publications (e.g. <https://www.pnas.org/doi/full/10.1073/pnas.240476612> 1 but also others) on ocean intrusion within the grounding zone, possibly by expanding some of the related discussion in section 5.2. Your comments on the absence of elevation thinning in these sectors for example seem particularly relevant.

## 5.1 Basal Melt Rates

Aside from some differences in magnitude, the general patterns of persistent HB retreat and rapid ice-column thinning and basal melt along the TGIS grounding zoneGZ that we observe are in agreement with other recent observations (e.g. Holland et al., 2023; Milillo et al., 2019; Schmidt et al., 2023; Adusumilli et al., 2020). All confirm that  $M_b$  is consistently smaller in magnitude on the TEIS than the TWIT, and that more basal melting occurs near the grounding zoneGZ than further seaward. Others have also observed and modelled rapid and potentially unstable retreat of the grounding zoneGZ, attributed to enhanced basal-ice-shelf melting (Joughin et al., 2014; Rignot et al., 2014; Seroussi et al., 2017; Yu et al., 2018; Milillo et al., 2019; Hoffman et al., 2019). Enhanced basal melt rates are in turn attributed to the intrusion of warm Circumpolar Deep Water (CDW) flowing along bathymetric troughs to the grounding zoneGZ (Nakayama et al., 2018; Milillo et al., 2019; Hogan et al., 2020). In the TGIS region, CDW intrusion primarily occurs along two bathymetric troughs (indicated in Fig. 1), allowing it to reach the grounding zoneGZ of both the TEIS and the TWIT (Dutrieux et al., 2014; Dotto et al., 2022).

The modest basal melt rates that we observe in the vicinity of Cavities 1, 1a, and 2 (Fig. 3d–f) are largely in agreement with those observed by the Icefin submersible in the same region (Schmidt et al., 2023). Holland et al. (2023) show modest apparent basal mass gain along the eastern and southern flankGZs of the TWIT main trunkembayment in 2011 and basal melt rates reaching 250 m  $\text{yr}^{-1}\text{a}^+$  along the southwestern boundary in both 2011 and 2022. High rates of apparent basal mass gain in the TWIT main trunk are also inferred by Milillo et al. (2019). We observe basal melt rates reaching  $\sim 250$  m  $\text{yr}^{-1}\text{a}^+$  throughout the main trunkTWIT, especially at the southwestern flank-of-the-main-trunk-GZ, but we observe no basal mass gain at the southern flankGZ. We suggest that the choice of Lagrangian flow-shifting methods can result in apparent mass gain in the TWIT if the time-evolving flow divergence is not accounted for (Fig. S9). Milillo et al. (2019) posit that, as the ice thins and the grounding line retreats, the bending zone where the ice is deflected below flotation before rebounding also retreats, causing changes at the surface to mask the true magnitude of ice thinning and overestimate  $M_b$ . With the caveat that BedMachine is poorly constrained in this ice-shelf cavity (Fig. S8) we also see intermittent re-grounding of ice in the raw HB features (Figs. 5b, S4d), which would further complicate the actual hydrostatic rebound, as well as the hydrostatic assumption and assumptions about ice flow. These factors all reduce confidence in the inferred  $DHE/Dt$  and  $M_b$  in the TWIT main trunkembayment. While we do not estimate melt rates below grounded ice, we observe a few regions where isolated HBs inland of the continental HB are aligned or collocated with inferred subglacial channels and regions of grounded ice thinning (e.g. in and around Cavities 1a, 6, 8, and 9); these resemble regions of uplift and subsidence mapped by Rignot et al. (2024) which may indicate enhanced subglacial melting upstream of the grounding zone and are discussed further in Section 5.2.

## 5.2 Hydrostatic Boundaries

In agreement with other studies, we find a mix of stagnation and retreat of the HB along the entire coast of the TGIS. The fastest retreat rates are collocated with retrograde slopes in the bed topography, ice-shelfbasal channels that intersect the IPY GL and/or the positions of inferred subglacial channels, and high basal melt rates. Notably, our  $M_b$  estimates and HB

Commented [36]: R2 "Rapid thinning" in a Lagrangian sense has a different meaning than the general understanding of ice shelf thinning. I would urge caution. Somewhere in the manuscript it would be good to articulate what can lead to ice shelf thinning in a Lagrangian reference frame, and in the discussion to address the plausibility of various processes.

Commented [37]: R2 "Rapid thinning" in a Lagrangian sense has a different meaning than the general understanding of ice shelf thinning. I would urge caution. Somewhere in the manuscript it would be good to articulate what can lead to ice shelf thinning in a Lagrangian reference frame, and in the discussion to address the plausibility of various processes.



613 retreat for the fast-flowing TWIT main trunk align closely with several other studies; we find HB retreat rates of 0.3–0.6 km  
614 yr<sup>-1</sup> between 2011–2019 and basal melt rates reaching 180 m yr<sup>-1</sup> as Cavity 9 opened along the western flank. Notably, our  
615 rates of thinning and HB retreat for the fast-flowing TWIT main trunk align closely with those of Milillo et al. (2019), who  
616 showed that the grounding line along the western flank margin of the TWIT embayment (what we call Cavity 9; near points A  
617 and B in Fig. 1 in Milillo et al. (Milillo et al., 2019)) retreated at a rate of 0.6 km yr<sup>-1</sup> to the west between 2011 and 2017.  
618 Our results also align with those of Bevan et al. (2021), who documented the opening of an ice-shelf cavity along the retreating  
619 western flank margin between 2014 and 2017, and Rignot et al. (2024), who observe a retreat rate of about 0.5 km yr<sup>-1</sup> between  
620 2018–2023 in this region. We also find HB retreat rates of 0.3–0.6 km a<sup>-1</sup> between 2011–2019 and basal melt rates reaching  
621 180 m a<sup>-1</sup> as Cavity 9 opened. Milillo et al. (2019) attributed the rapid ungrounding at their point labelled “A” in their figures  
622 (which falls within Cavity 9) to its prograde slope, which favours CDW intrusion and efficient cavity opening, consistent with  
623 plume theory (Jenkins, 2011).

624 ThC2, ThC3, ThC5, and SD3 are associated with Type 1 HB retreat in narrow bands oblique to the flow direction,  
625 but parallel to inferred subglacial channels, lending confidence to our predicted subglacial channel distribution and indicating  
626 that subglacial melting is strong (Figs. 3–5). Similar retreat along subglacial channels has been observed on  
627 Nioghalvfjerdingsfjorden Glacier (N79) Ice Tongue in northeast Greenland (Narkevic et al., 2023) and the Petermann Glacier Ice  
628 Tongue in northwest Greenland (Ciraci et al., 2023), although in both cases, retreat occurred in narrow bands aligned with the  
629 direction of ice flow. Hager et al. (2022) showed that the inclusion of channelized drainage into their model increased effective  
630 pressures in non-channelized regions near the grounding line, which may increase basal drag and reduce grounding line retreat  
631 and mass loss (Yu et al., 2018) and velocities on Pine Island Glacier (Gillet-Chaulet et al., 2016; Joughin et al., 2019). We  
632 observe little to no retreat where subglacial channelization is not present, which may be due to high points or prograde slopes  
633 in the bed topography but could possibly be due in part to enhanced basal friction in the absence of subglacial water or its  
634 concentration within subglacial channels. It is expected that subglacial melt rates are higher where discharge of subglacial  
635 meltwater occurs (e.g. Le Brocq et al., 2013; Washam et al., 2019). The basal meltwater volume from basal melt has been  
636 estimated at 3.5 Gt yr<sup>-1</sup> for the 189,000 km<sup>2</sup> Thwaites Glacier drainage basin, with most of the melt occurring within about  
637 50 km of the grounding zone (GZ) surface velocities exceed 500 m a<sup>-1</sup> (Joughin et al., 2009). Our study area extends from ~10–  
638 100 km inland of the grounding zone (GZ), so ample subglacial water is available, and may discharge in the manner we predict  
639 (Figs. 3–5a, S4b), forming a collection of ice-shelf basal channels when it reaches the ice shelf (Section 5.3). While we do not  
640 investigate evolution of the subglacial cumulative drainage area over time, we posit that any discrepancies in orientation or  
641 position among mapped surface depressions and basal incisions may be due to rerouting of the subglacial drainage system.

642 In contrast with the retreat observed along the continuous continental grounding zone (GZ) and shrinking or  
643 ungrounding of pinning points 1, 2, and 3, PP4 and PP5 exhibit signs of growth throughout the study period, particularly with  
644 advance to the northwest of their IPY positions (Figs. 1, S4). Indeed, the bed topographic high on which these pinning points  
645 rest extends and grows taller to the northwest (Fig. S8a), and some localised thickening is observed as the TEIS flows onto  
646 PP5, although the region is dominated by ice-column thinning and basal melting (Fig. 2). Due to gaps in coverage (Fig. S2), it

Commented [38]: R1 “volume of basal melt .. 3.5Gt”. Please give a time period as well as an area. To claim this as “ample” requires some more data or argumentation.

Commented [39]: R1 Figure S8a would need some more annotation to support this statement.

647 is difficult to tell whether the ice—shelf area to the north of the pinning points is changing. Wild et al. (2022) demonstrate that  
648 although PP5 is structurally sounder than PP4, the two used to be connected and their separation and the disconnection of the  
649 TEIS and TWIT has altered ice flow. This change, along with the advection of thinner and more damaged ice on the TEIS  
650 portends ungrounding from the pinning point within the next decade (Wild et al., 2022).

651 The unfiltered and unsmoothed HBs observed throughout the Thwaites Glacier and TGIS provide insight into  
652 potential future behaviour. We observe isolated HBs inlandupstream of the continental grounding zoneGZ, indicating that the  
653 ice surface is below the “hydrostatic grounding height” (ice surface height resulting from adding the flotation thickness  $H_E$  for  
654 all ice to the bed height, Figs. 3–5b–c) above bedrock lows. The bed heights from BedMachine v3 are relatively reliable inland  
655 upstream of the IPY GL, with errors < 50 m (Fig. S8b), which is similar to the uncertainty in our calculation of  $H_E$ , promoting  
656 confidence in the existence of pockets where the surface is below the hydrostatic grounding height inlandupstream of the  
657 grounding zoneGZ. Several of the isolated HBs inlandupstream of the grounding zoneGZ persist over multiple epochs and  
658 align with inferred subglacial drainage pathways. The isolated HBs inlandupstream of the IPY GL are necessarily located at  
659 bed topographic lows, and likely contribute to the cycle of rapid retreat and temporary stabilisation observed along several  
660 reference channels. Indeed, Figures 3–5b show that the continental HB retreated far enough for several cavities to encompass  
661 some of these isolated HBs from earlier epochs. Notably, the grounding zoneGZ near ThC6, which aligns with the inferred  
662 subglacial channel location with the highest flow accumulation, experienced modest HB retreat but high rates of grounded ice  
663 thinning and ice—shelf basal melting and ice-column thinning (Fig. 5), potentially foreshadowing the formation of a Type 2  
664 cavity; however, there are few isolated HBs further inlandupstream (Fig. 5b–c). ~~Furthermore, high rates of thinning in the  
665 vicinity of a few of these upstream HBs (in and around Cavities 1a, 6, 8, and 9) may indicate ocean-induced melting above  
666 the GZ, as observed on Petermann Glacier (Gadi et al., 2023). We do not observe any increased melt rates or thinning for most  
667 of these closed regions, however, even when they are near the main HB, suggesting there is little incursion of seawater that  
668 might enhance melt for most of the glacier.~~

669 We also observe isolated HBs throughout the TWIT, indicating that the ice surface is above the hydrostatic grounding  
670 height above bedrock highs (Figs. 3–5b–c). In contrast to our certainty in mapping isolated HBs above the grounding zoneGZ,  
671 BedMachine errors increase rapidly to 400 m downstream of the IPY GL, where the bed is inferred from gravity inversion, so  
672 we are less confident in the existence of additional pinning points within the TGIS, with the exception of the “HR” ice rumple  
673 which was independently mapped by Holland et al. (2023) using similar methods (Fig. 5b). We expect that the isolated HBs  
674 that persist on high points within ~2 km downstream of the IPY GL throughout several years (where BedMachine errors are  
675 around 100 m, Fig. S8b), may have been or currently are pinning points. Likewise, we expect sufficiently high points between  
676 the isolated HBs inlandupstream of the grounding zoneGZ (Figs. 3–5b, S8) to serve as temporary pinning points as new cavities  
677 open around them as the continental HB retreats.

Commented [40]: R2 Could you discuss the implication of this magnitude of error on the smooth annual HB? Could this explain some of the discrepancy with the IPY GL in the TWIT sector (fig. 5)?

### 5.3 Ice-shelfBasal Channels

Based on our inferred subglacial drainage pattern and mapped surface depressions and basal incisions, we suggest that all ice-shelfbasal channels identified in this study except ThC4 are subglacially sourced. Ice-shelfbasal channels have been mapped previously on the TGIS by Alley et al. (2016), and several subglacial channels were also identified by Milillo et al. (2019), many of which align with our DSM-derived channel positions. Comparisons between these observations provide insights into the formation of each ice-shelfbasal channel.

There is relatively strong evidence that ThC1 is a subglacially-sourced ice-shelfbasal channel. The downstream end of ThC1 is about 6 km away from an ice-shelfbasal channel identified by Alley et al. (2016) (Fig. S10), and its inlandupstream end roughly aligns with where Milillo et al. (2019) document the formation of an approximately 1 km wide subglacial channel near Cavities 1, 1a, and 2 (points C and D from Fig. 1 in Milillo et al. (2019)) before the grounding line retreated to its 2017 extent. They observed no change in velocity along the subglacial channel, and thus attribute thinning in this region to ocean-induced basal melting rather than dynamic thinning (Milillo et al., 2019; Millgate et al., 2013). Schmidt et al. (2023) confirmed strong basal melting in this region, with the fastest rates along the steep slopes of terraces at the ice-shelf base, consistent with observations at Pine Island Glacier (Dutrieux et al., 2014). Although Schmidt et al. (2023) did not sample at the location of ThC1, their finding that the greatest basal melting occurs along steep basal slopes in this region provides further evidence that ThC1 is a subglacially-sourced channel whose steep sides promote high basal melt rates and retreat along its trunk.

Two channels mapped by Alley et al. (2016) roughly align with the locations of ThC3 and ThC4, and a third runs parallel to the end of ThC7 but begins further downstream (Fig. S10). Alley et al. (2016) considered the ice-shelfbasal channels parallel to ThC4 and ThC7 to be subglacially sourced. Our observations support this claim for ThC7 but suggest that ThC4 may be a grounding-linezone sourced incision as ice flows over local bedrock topographic highs as described in Sections 4.2.2 (Fig. 5), although we cannot confirm whether it entrains buoyant plumes. Furthermore, the retreat along SD3 also appears to be coincident with a subglacial drainage channel modelled and mapped by Hager et al. (2022, Figure 5), although due to the breakdown of the hydrostatic assumption in the TWIT main trunk, we cannot confirm whether this inferred subglacial channel forms an ice-shelfbasal channel in the ice shelf.

One of the channels we observe, ThC7, initiates near where two subglacial drainage channels discharge to the ocean (Rignot et al., 2024). Using differential SAR interferometry, Rignot et al. (2024) observed several circular areas ~4–6 km in diameter with time-varying uplift and subsidence (10–20 cm). These features are located above subglacial topographic depressions that abut km-scale subglacial ridges. The major features are all adjacent to prominent subglacial drainage channels and resemble the isolated HBS we infer inland of the grounding zoneGZ in and around Cavities 1a, 6, 8, and 9 (Figs. 3–5b). Rignot et al. (2024) conclude that the filling and draining of the more inland features is driven by fluctuations in the subglacial water flow through the nearby channels. For the large ‘bull’s eye’ feature just ~6 km above the grounding zone (see Figure 4c in Rignot et al. 2024), however, they speculate that the vertical motion is due to tidally-forced seawater intrusion, which they suggest should cause enhanced subglacial melting. They do not specify the magnitude of this melt other than to say it should

711 be much lower than 20 m yr<sup>-1</sup>. If this non-steady melting is significantly above the background subglacial melt rate, we would  
712 expect to see a signature in the long-term thinning rates. Instead, the 2020–2023 elevation change data show thinning of 1–2  
713 m yr<sup>-1</sup> in the area surrounding the feature near ThC7 with minor thickening (< 0.5 m yr<sup>-1</sup>) near its centre in 2020–2023,  
714 providing little or no indication of enhanced subglacial melt (Figs. 5, S7). We also note that dH/dt derived from annual DSM  
715 mosaics does not provide the fine temporal resolution (up to sub-daily) over which uplift/subsidence features were observed  
716 in this study. We do not observe increased rates of thinning for most of these closed regions, even when they are near the main  
717 HB, suggesting that any enhanced subglacial melting due to incursion of seawater may not persist long enough to significantly  
718 impact the signal on multi-annual timescales for most of the glacier. Furthermore, Bradley and Hewitt (2024) show through  
719 modelling that Thwaites Glacier is likely not susceptible to runaway melting as a result of seawater intrusion processes. An  
720 alternate hypothesis is that all of the circular features are driven by subglacial water flow rather than seawater intrusion. This  
721 hypothesis is supported by a strong gradient in the hydraulic potential between the grounding zone and the ‘bull’s eye’ feature,  
722 which should drive the water toward – not away from – the ocean (Fig. S6). Seawater intrusion is also problematic because it  
723 needs to occur over an area where the predominant flow direction should be seaward to accommodate major subglacial  
724 outflows. These features likely fill and drain through exchange of water with the adjacent subglacial channels, similar to how  
725 lakes located much farther inland fill and drain below Thwaites Glacier (Smith et al., 2017) and Jutulstraumen Glacier (Neckel  
726 et al., 2021). If this is the case, the pressure boundary condition where these channels meet the ocean should be subject to tidal  
727 modulation (10 kPa) sufficient to explain the observed ~10–20 cm uplift/subsidence (1–2 kPa).  
728

## 729 **6 Conclusions**

730 This study presents novel, time-evolving rates of ice-shelf thickness and basal mass change and proxies for grounding line  
731 and ice-shelfbasal channel position on the TGIS derived from high resolution REMA DSM products, providing further  
732 evidence linking high basal melt rates along ice-shelfbasal channels to rapid rates of grounding-zone retreat (e.g. Narkevic  
733 et al., 2023; Holland et al., 2023; Ciraci et al., 2023). Hydrostatic boundary retreat rates averaging 0.6 km yr<sup>-1</sup>a<sup>+</sup> and at times  
734 > 3 km yr<sup>-1</sup>a<sup>+</sup> were observed concurrently with persistent ice-shelfbasal channels and basal melt rates as high as 250 m yr<sup>-1</sup>  
735 a<sup>+</sup>. The retreat is not fully attributable to the presence of ice-shelfbasal channels, as several regions where HB retreated along  
736 reference channels also had deep retrograde bed slopes and/or were likely to be in contact with warm CDW. This study does  
737 not deconvolve all potential causes and effects of HB retreat, such as changes in ice velocity through time (e.g. dos Santos et  
738 al., 2021), varying subglacial discharge (e.g. Hager et al., 2022), or changing ocean currents (e.g. Holland et al., 2023; Dotto  
739 et al., 2022), but supports the hypothesis that ice-shelfbasal channels, whether initiated at the grounding zoneGZ or  
740 subglacially, are associated with more rapid grounding zoneGZ retreat than non-channelized areas. Our observations are  
741 consistent with other work that suggests buoyant meltwater plumes can entrain CDW to form plumes with strong basal melting  
742 capabilities (e.g. Le Brocq et al., 2013).

743 These results also provide additional evidence for the recent opening of new ice-shelf cavities not associated with  
744 ice-shelf basal channels, as observed by Milillo et al. (2019), Bevan et al. (2021), and Schmidt et al. (2023), and point to the  
745 potential for continued, unstable retreat of the grounding line zone (e.g. Yu et al., 2018; Joughin et al., 2014), particularly along  
746 inferred subglacial drainage pathways. As the grounding zone GZ continues to retreat and subglacial pressures change, we  
747 suggest that retreat along existing and/or rerouted subglacial channels that intersect the grounding zone GZ will continue to  
748 form narrow, Type 2 cavities in the future, complicating the task of accurately predicting future grounding zone GZ retreat.

749 Milillo et al. (2019) point out that several of the newly opened ice-shelf cavities have less than 100 m between the  
750 ice-shelf base and the sea floor, and to simulate these basal melt and retreat processes would require a significantly finer  
751 spatial resolution than is currently available to ocean models. This methodology can be applied to other ice shelves to further  
752 investigate the prevalence of HB retreat at channelized and non-channelized grounding zones to further investigate relevant  
753 changes in ice-shelf structure, velocity, basal and subglacial melt rates, and subglacial drainage. This study is an important  
754 step towards better understanding these complex and critical regions of the Antarctic ice sheet and the relevant temporal and  
755 spatial scales over which these processes occur.

#### 756 Code and Data Availability

757 REMA v4.1 2 m strips (DOI:10.7910/DVN/X7NDNY) and 200 m mosaics (DOI: 10.7910/DVN/EBW8UC) are available at  
758 the Polar Geospatial Center. The following datasets are available at NSIDC DAAC: BedMachine Antarctica V003 bed heights,  
759 firm and ice thicknesses, Eigen-6C4 geoid data (DOI: 10.5067/FPSU0V1MWUB6), MEaSURES Antarctic Boundaries for  
760 IPY 2007–2009 from Satellite Radar V002 (DOI: 10.5067/AXE4121732AD), MEaSURES Antarctic Grounding Line from  
761 Differential Satellite Radar Interferometry V002 (DOI: 10.5067/IKBWW4RYHF1Q), MEaSURES InSAR-Based Antarctica  
762 Ice Velocity Map V002 (DOI: 10.5067/D7GK8F5J8M8R), MEaSURES Annual Antarctic Ice Velocity Maps V001 (DOI:  
763 10.5067/9T4EPQXTJYW9), ATLAS/ICESat-2 L3A Land Ice Height V005 (DOI: 10.5067/ATLAS/ATL06.005) and V006  
764 (DOI: 10.5067/ATLAS/ATL06.006), IceBridge MCoRDS L2 Ice Thickness V001 (DOI: 10.5067/GDQ0CUCVTE2Q),  
765 IceBridge ATM L1B Elevation and Return Strength V002 (DOI: 10.5067/19SIM5TXKPGT), IceBridge LVIS-GH L2  
766 Geolocated Surface Elevation Product V001 (DOI: 10.5067/RELPCEXB0MY3), and IceBridge Riegl Laser Altimeter L2  
767 Geolocated Surface Elevation Triplets V001 (DOI: 10.5067/JV9DENETK13E). The DTU22 MDT model is available at  
768 (2019). The CATS2008b tide model (DOI: 10.15784/601235) is available at USAP-DC. RACMO 3p2 data are available at  
769 [https://www.projects.science.uu.nl/iceclimate/publications/data/2018/vwessem2018\\_tc/RACMO\\_Yearly/](https://www.projects.science.uu.nl/iceclimate/publications/data/2018/vwessem2018_tc/RACMO_Yearly/). TopoToolbox  
770 v2.3.1 is available on the Mathworks File Exchange.

771 All code, gridded products generated in this study (annual mosaics, annual velocities derived from the Amundsen Sea  
772 quarterly velocities, and rates of change), and shapefiles of the reference channels and annual HBs will be made freely available  
773 with a permanent DOI at Zenodo by the time of final publication. In the interim, near-final versions are available at DOI:  
774 10.5281/zenodo.10969572.

775 **Author Contributions**

776 AC conceived the ideas and carried out analyses with support from IH. IH created the annual REMA DSM mosaics, IJ provided  
777 the quarterly velocity maps for the Amundsen Sea regions, and BS performed the CryoSat-2 registrations for the REMA DSM  
778 strips. AC prepared the manuscript with contributions from all authors.

779 **Competing Interests**

780 Some authors are members of the editorial board of *The Cryosphere*.

781 **Acknowledgements**

782 Allison Chartrand and Ian Howat were funded by the National Aeronautics and Space Administration (NASA:  
783 80NSSC20K1658), the National Science Foundation (NSF: Award No. 2217574), and the Ohio State University. Ian Joughin  
784 was funded by NASA Grant 80NSSC20K0954.

785 **References**

- 786 Adusumilli, S., Fricker, H. A., Medley, B., Padman, L., and Siegfried, M. R.: Interannual variations in meltwater input to the  
787 Southern Ocean from Antarctic ice shelves, *Nat. Geosci.*, 13, 616–620, <https://doi.org/10.1038/s41561-020-0616-z>,  
788 2020.
- 789 Alley, K. E., Scambos, T. A., Siegfried, M. R., and Fricker, H. A.: Impacts of warm water on Antarctic ice shelf stability  
790 through basal channel formation, *Nature Geosci.*, 9, 290–293, <https://doi.org/10.1038/ngeo2675>, 2016.
- 791 Alley, K. E., Scambos, T. A., Alley, R. B., and Holschuh, N.: Troughs developed in ice-stream shear margins precondition ice  
792 shelves for ocean-driven breakup, *Science Advances*, 5, eaax2215, <https://doi.org/10.1126/sciadv.aax2215>, 2019.
- 793 Bevan, S. L., Luckman, A. J., Benn, D. I., Adusumilli, S., and Crawford, A.: Brief communication: Thwaites Glacier cavity  
794 evolution, *The Cryosphere*, 15, 3317–3328, <https://doi.org/10.5194/tc-15-3317-2021>, 2021.
- 795 Blair, J. B. and Hofton, M.: IceBridge LVIS-GH L2 Geolocated Surface Elevation Product, Version 1,  
796 <https://doi.org/10.5067/RELPCEXB0MY3>, 2015.
- 797 Blankenship, D. D., Kempf, S., Young, D. A., Roberts, J. L., van Ommen, T., Forsberg, R., Siegert, M., Palmer, S. J., and  
798 Dowdeswell, J. A.: IceBridge Riegl Laser Altimeter L2 Geolocated Surface Elevation Triplets, Version 1,  
799 <https://doi.org/10.5067/JV9DENETK13E>, 2012.
- 800 [Bradley, A. T. and Hewitt, I. J.: Tipping point in ice-sheet grounding-zone melting due to ocean water intrusion, \*Nat. Geosci.\*,  
801 17, 631–637, <https://doi.org/10.1038/s41561-024-01465-7>, 2024.](https://doi.org/10.1038/s41561-024-01465-7)
- 802 Chartrand, A. M. and Howat, I. M.: Basal Channel Evolution on the Getz Ice Shelf, West Antarctica, *J. Geophys. Res. Earth*  
803 *Surf.*, 125, <https://doi.org/10.1029/2019JF005293>, 2020.
- 804 Chartrand, A. M. and Howat, I. M.: A comparison of contemporaneous airborne altimetry and ice-thickness measurements of  
805 Antarctic ice shelves, *Journal of Glaciology*, 1–14, <https://doi.org/10.1017/jog.2023.49>, 2023.
- 806 Ciraci, E., Rignot, E., Scheuchl, B., Tolpekin, V., Wollersheim, M., An, L., Milillo, P., Bueso-Bello, J.-L., Rizzoli, P., and  
807 Dini, L.: Melt rates in the kilometer-size grounding zone of Petermann Glacier, Greenland, before and during a retreat,  
808 *Proceedings of the National Academy of Sciences*, 120, e2220924120, <https://doi.org/10.1073/pnas.2220924120>,  
809 2023.

810 Dotto, T. S., Heywood, K. J., Hall, R. A., Scambos, T. A., Zheng, Y., Nakayama, Y., Hyogo, S., Snow, T., Wählin, A. K.,  
811 Wild, C., Truffer, M., Muto, A., Alley, K. E., Boehme, L., Bortolotto, G. A., Tyler, S. W., and Pettit, E.: Ocean  
812 variability beneath Thwaites Eastern Ice Shelf driven by the Pine Island Bay Gyre strength, *Nat Commun*, 13, 7840,  
813 <https://doi.org/10.1038/s41467-022-35499-5>, 2022.

814 Dow, C. F., Lee, W. S., Greenbaum, J. S., Greene, C. A., Blankenship, D. D., Poinar, K., Forrest, A. L., Young, D. A., and  
815 Zappa, C. J.: Basal channels drive active surface hydrology and transverse ice shelf fracture, *Science Advances*, 4,  
816 eaao7212, <https://doi.org/10.1126/sciadv.aao7212>, 2018.

817 Drews, R.: Evolution of ice-shelf channels in Antarctic ice shelves, *The Cryosphere*, 9, 1169, <https://doi.org/10.5194/tc-9-1169-2015>, 2015.

818 Drews, R., Pattyn, F., Hewitt, I. J., Ng, F. S. L., Berger, S., Matsuoka, K., Helm, V., Bergeot, N., Favier, L., and Neckel, N.:  
819 Actively evolving subglacial conduits and eskers initiate ice shelf channels at an Antarctic grounding line, *Nature*  
820 *Communications*, 8, 1–10, <https://doi.org/10.1038/ncomms15228>, 2017.

821 Dutrieux, P., De Rydt, J., Jenkins, A., Holland, P. R., Ha, H. K., Lee, S. H., Steig, E. J., Ding, Q., Abrahamsen, E. P., and  
822 Schröder, M.: Strong Sensitivity of Pine Island Ice-Shelf Melting to Climatic Variability, *Science*, 343, 174–178,  
823 <https://doi.org/10.1126/science.1244341>, 2014.

824 European Space Agency: L1b NOP-IOP-GOP SAR, Version Baseline C., <https://doi.org/10.5270/CR2-gsyvnx0>, 2023.

825 Förste, C., Bruinsma, Sean L., Abrikosov, O., Lemoine, J.-M., Marty, J. C., Flechtner, F., Balmino, G., Barthelmes, F., and  
826 Biancale, R.: EIGEN-6C4 The latest combined global gravity field model including GOCE data up to degree and  
827 order 2190 of GFZ Potsdam and GRGS Toulouse, <https://doi.org/10.5880/ICGEM.2015.1>, 2014.

828 Gadi, R., Rignot, E., and Menemenlis, D.: Modeling Ice Melt Rates From Seawater Intrusions in the Grounding Zone of  
829 Petermann Gletscher, Greenland, *Geophysical Research Letters*, 50, e2023GL105869,  
830 <https://doi.org/10.1029/2023GL105869>, 2023.

831 Gillet-Chaulet, F., Durand, G., Gagliardini, O., Mosbeux, C., Mouginit, J., Rémy, F., and Ritz, C.: Assimilation of surface  
832 velocities acquired between 1996 and 2010 to constrain the form of the basal friction law under Pine Island Glacier,  
833 *Geophysical Research Letters*, 43, 10,311-10,321, <https://doi.org/10.1002/2016GL069937>, 2016.

834 Goldberg, D. N., Heimbach, P., Joughin, I., and Smith, B.: Committed retreat of Smith, Pope, and Kohler Glaciers over the  
835 next 30 years inferred by transient model calibration, *The Cryosphere*, 9, 2429–2446, <https://doi.org/10.5194/tc-9-2429-2015>, 2015.

836 Gourmelen, N., Goldberg, D. N., Snow, K., Henley, S. F., Bingham, R. G., Kimura, S., Hogg, A. E., Shepherd, A., Mouginit,  
837 J., Lenaerts, J. T. M., Ligtenberg, S. R. M., and Berg, W. J. van de: Channelized Melting Drives Thinning Under a  
838 Rapidly Melting Antarctic Ice Shelf, *Geophysical Research Letters*, 44, 9796–9804,  
839 <https://doi.org/10.1002/2017GL074929>, 2017.

840 Gudmundsson, G. H., Krug, J., Durand, G., Favier, L., and Gagliardini, O.: The stability of grounding lines on retrograde  
841 slopes, *The Cryosphere*, 6, 1497–1505, <https://doi.org/10.5194/tc-6-1497-2012>, 2012.

842 Hager, A. O., Hoffman, M. J., Price, S. F., and Schroeder, D. M.: Persistent, extensive channelized drainage modeled beneath  
843 Thwaites Glacier, West Antarctica, *The Cryosphere*, 16, 3575–3599, <https://doi.org/10.5194/tc-16-3575-2022>, 2022.

844 Hoffman, M. J., Asay-Davis, X., Price, S. F., Fyke, J., and Perego, M.: Effect of Subshelf Melt Variability on Sea Level Rise  
845 Contribution From Thwaites Glacier, Antarctica, *Journal of Geophysical Research: Earth Surface*, 124,  
846 e2019JF005155, <https://doi.org/10.1029/2019JF005155>, 2019.

847 Hogan, K. A., Larter, R. D., Graham, A. G. C., Arthern, R., Kirkham, J. D., Totten, R. L., Jordan, T. A., Clark, R., Fitzgerald,  
848 V., Wählin, A. K., Anderson, J. B., Hillenbrand, C.-D., Nitsche, F. O., Simkins, L., Smith, J. A., Gohl, K., Arndt, J.  
849 E., Hong, J., and Wellner, J.: Revealing the former bed of Thwaites Glacier using sea-floor bathymetry: implications  
850 for warm-water routing and bed controls on ice flow and buttressing, *The Cryosphere*, 14, 2883–2908,  
851 <https://doi.org/10.5194/tc-14-2883-2020>, 2020.

852 Holland, P. R., Bevan, S. L., and Luckman, A. J.: Strong Ocean Melting Feedback During the Recent Retreat of Thwaites  
853 Glacier, *Geophysical Research Letters*, 50, e2023GL103088, <https://doi.org/10.1029/2023GL103088>, 2023.

854 Howat, I. M., Porter, C., Smith, B. E., Noh, M.-J., and Morin, P.: The Reference Elevation Model of Antarctica, *The*  
855 *Cryosphere*, 13, 665–674, <https://doi.org/10.5194/tc-13-665-2019>, 2019.

856 Jenkins, A.: Convection-Driven Melting near the Grounding Lines of Ice Shelves and Tidewater Glaciers, *J. Phys. Oceanogr.*,  
857 41, 2279–2294, <https://doi.org/10.1175/JPO-D-11-03.1>, 2011.



860 Joughin, I., Tulaczyk, S., Bamber, J. L., Blankenship, D., Holt, J. W., Scambos, T., and Vaughan, D. G.: Basal conditions for  
861 Pine Island and Thwaites Glaciers, West Antarctica, determined using satellite and airborne data, *Journal of*  
862 *Glaciology*, 55, 245–257, <https://doi.org/10.3189/002214309788608705>, 2009.

863 Joughin, I., Smith, B. E., and Medley, B.: Marine Ice Sheet Collapse Potentially Under Way for the Thwaites Glacier Basin,  
864 West Antarctica, *Science*, 344, 735–738, <https://doi.org/10.1126/science.1249055>, 2014.

865 Joughin, I., Smith, B. E., and Schoof, C. G.: Regularized Coulomb Friction Laws for Ice Sheet Sliding: Application to Pine  
866 Island Glacier, Antarctica, *Geophysical Research Letters*, 46, 4764–4771, <https://doi.org/10.1029/2019GL082526>,  
867 2019.

868 Joughin, I., Shapero, D., and Dutrieux, P.: Responses of Pine Island and Thwaites Glaciers to Melt and Sliding  
869 Parameterizations, *EGUphere*, 1–34, <https://doi.org/10.5194/egusphere-2023-2929>, 2024.

870 Knudsen, P., Andersen, O., and Maximenko, N.: A new ocean mean dynamic topography model, derived from a combination  
871 of gravity, altimetry and drifter velocity data, *Advances in Space Research*, 68, 1090–1102,  
872 <https://doi.org/10.1016/j.asr.2019.12.001>, 2021.

873 Le Brocq, A. M., Ross, N., Griggs, J. A., Bingham, R. G., Corr, H. F. J., Ferraccioli, F., Jenkins, A., Jordan, T. A., Payne, A.  
874 J., Rippin, D. M., and Siegert, M. J.: Evidence from ice shelves for channelized meltwater flow beneath the Antarctic  
875 Ice Sheet, *Nature Geoscience*, 6, 945–948, <https://doi.org/10.1038/ngeo1977>, 2013.

876 Ligtenberg, S. R. M., Helsen, M. M., and Broeke, M. R. van den: An improved semi-empirical model for the densification of  
877 Antarctic firn, *The Cryosphere*, 5, 809–819, <https://doi.org/10.5194/tc-5-809-2011>, 2011.

878 [Miles, B. W. J., Stokes, C. R., Jenkins, A., Jordan, J. R., Jamieson, S. S. R., and Gudmundsson, G. H.: Intermittent structural](#)  
879 [weakening and acceleration of the Thwaites Glacier Tongue between 2000 and 2018, \*Journal of Glaciology\*, 66, 485–](#)  
880 [495, <https://doi.org/10.1017/jog.2020.20>, 2020.](#)

881 Milillo, P., Rignot, E., Rizzoli, P., Scheuchl, B., Mouginot, J., Bueso-Bello, J., and Prats-Iraola, P.: Heterogeneous retreat and  
882 ice melt of Thwaites Glacier, West Antarctica, *Science Advances*, 5, eaau3433,  
883 <https://doi.org/10.1126/sciadv.aau3433>, 2019.

884 Millgate, T., Holland, P. R., Jenkins, A., and Johnson, H. L.: The effect of basal channels on oceanic ice-shelf melting, *Journal*  
885 *of Geophysical Research: Oceans*, 118, 6951–6964, <https://doi.org/10.1002/2013JC009402>, 2013.

886 Morlighem, M.: MEaSURES BedMachine Antarctica, Version 3, 2022.

887 Morlighem, M., Rignot, E., Binder, T., Blankenship, D., Drews, R., Eagles, G., Eisen, O., Ferraccioli, F., Forsberg, R.,  
888 Fretwell, P., Goel, V., Greenbaum, J. S., Gudmundsson, H., Guo, J., Helm, V., Hofstede, C., Howat, I., Humbert, A.,  
889 Jokat, W., Karlsson, N. B., Lee, W. S., Matsuoka, K., Millan, R., Mouginot, J., Paden, J., Pattyn, F., Roberts, J.,  
890 Rosier, S., Ruppel, A., Seroussi, H., Smith, E. C., Steinhage, D., Sun, B., Broeke, M. R. van den, Ommen, T. D. van,  
891 Wessem, M. van, and Young, D. A.: Deep glacial troughs and stabilizing ridges unveiled beneath the margins of the  
892 Antarctic ice sheet, *Nature Geoscience*, 13, 132–137, <https://doi.org/10.1038/s41561-019-0510-8>, 2020.

893 Mouginot, J., Scheuchl, B., and Rignot, E.: Mapping of Ice Motion in Antarctica Using Synthetic-Aperture Radar Data, *Remote*  
894 *Sensing*, 4, 2753–2767, <https://doi.org/10.3390/rs4092753>, 2012.

895 Mouginot, J., Scheuchl, B., and Rignot, E.: MEaSURES Annual Antarctic Ice Velocity Maps 2005–2017, Version 1, , Boulder,  
896 Colorado USA, 2017a.

897 Mouginot, J., Scheuchl, B., and Rignot, E.: MEaSURES Antarctic Boundaries for IPY 2007–2009 from Satellite Radar,  
898 Version 2, <https://doi.org/10.5067/AXE4121732AD>, 2017b.

899 Nakayama, Y., Menemenlis, D., Zhang, H., Schodlok, M., and Rignot, E.: Origin of Circumpolar Deep Water intruding onto  
900 the Amundsen and Bellingshausen Sea continental shelves, *Nature Communications*, 9, 3403,  
901 <https://doi.org/10.1038/s41467-018-05813-1>, 2018.

902 Narkevic, A., Csatho, B., and Schenk, T.: Rapid Basal Channel Growth Beneath Greenland’s Longest Floating Ice Shelf,  
903 *Geophysical Research Letters*, 50, e2023GL103226, <https://doi.org/10.1029/2023GL103226>, 2023.

904 [Neckel, N., Franke, S., Helm, V., Drews, R., and Jansen, D.: Evidence of Cascading Subglacial Water Flow at Jutulstraumen](#)  
905 [Glacier \(Antarctica\) Derived From Sentinel-1 and ICESat-2 Measurements, \*Geophysical Research Letters\*, 48,](#)  
906 [e2021GL094472, <https://doi.org/10.1029/2021GL094472>, 2021.](#)

907 Nuth, C. and Kääb, A.: Co-registration and bias corrections of satellite elevation data sets for quantifying glacier thickness  
908 change, *The Cryosphere*, 5, 271–290, <https://doi.org/10.5194/tc-5-271-2011>, 2011.

909 Paden, J. D., Li, J., Leuschen, C., Rodriguez-Morales, F., and Hale, R.: IceBridge MCoRDS L2 Ice Thickness, Version 1, ,  
910 Boulder, Colorado USA, 2010.

911 Paden, J. D., Li, J., Leuschen, Carl, Rodriguez-Morales, F., and Hale, R.: Pre-IceBridge MCoRDS L2 Ice Thickness, Version  
912 1, , Boulder, Colorado USA, 2011.

913 Padman, L., Siegfried, M. R., and Fricker, H. A.: Ocean Tide Influences on the Antarctic and Greenland Ice Sheets, *Rev.*  
914 *Geophys.*, 2016RG000546, <https://doi.org/10.1002/2016RG000546>, 2018.

915 Rignot, E., Mouginot, J., and Scheuchl, B.: Ice Flow of the Antarctic Ice Sheet, *Science*, 333, 1427–1430,  
916 <https://doi.org/10.1126/science.1208336>, 2011.

917 Rignot, E., Mouginot, J., Morlighem, M., Seroussi, H., and Scheuchl, B.: Widespread, rapid grounding line retreat of Pine  
918 Island, Thwaites, Smith, and Kohler glaciers, West Antarctica, from 1992 to 2011, *Geophysical Research Letters*, 41,  
919 3502–3509, <https://doi.org/10.1002/2014GL060140>, 2014.

920 Rignot, E., Mouginot, J., and Scheuchl, B.: MEaSURES Antarctic Grounding Line from Differential Satellite Radar  
921 Interferometry, Version 2, <https://doi.org/10.5067/KBWW4RYHF1Q>, 2016.

922 Rignot, E., Mouginot, J., and Scheuchl, B.: MEaSURES InSAR-Based Antarctica Ice Velocity Map, Version 2,  
923 <https://doi.org/10.5067/D7GK8F5J8M8R>, 2017.

924 Rignot, E., Mouginot, J., Scheuchl, B., van den Broeke, M., van Wessem, M. J., and Morlighem, M.: Four decades of Antarctic  
925 Ice Sheet mass balance from 1979–2017, *Proceedings of the National Academy of Sciences*, 116, 1095–1103,  
926 <https://doi.org/10.1073/pnas.1812883116>, 2019.

927 [Rignot, E., Ciraci, E., Scheuchl, B., Tolpekin, V., Wollersheim, M., and Dow, C.: Widespread seawater intrusions beneath the  
928 grounded ice of Thwaites Glacier, West Antarctica, \*Proceedings of the National Academy of Sciences\*, 121,  
929 e2404766121, <https://doi.org/10.1073/pnas.2404766121>, 2024.](https://doi.org/10.1073/pnas.2404766121)

930 dos Santos, T. D., Barnes, J. M., Goldberg, D. N., Gudmundsson, G. H., and Morlighem, M.: Drivers of Change of Thwaites  
931 Glacier, West Antarctica, Between 1995 and 2015, *Geophysical Research Letters*, 48, e2021GL093102,  
932 <https://doi.org/10.1029/2021GL093102>, 2021.

933 Schmidt, B. E., Washam, P., Davis, P. E. D., Nicholls, K. W., Holland, D. M., Lawrence, J. D., Riverman, K. L., Smith, J. A.,  
934 Spears, A., Dichek, D. J. G., Mullen, A. D., Clyne, E., Yeager, B., Anker, P., Meister, M. R., Hurwitz, B. C., Quartini,  
935 E. S., Bryson, F. E., Basinski-Ferris, A., Thomas, C., Wake, J., Vaughan, D. G., Anandakrishnan, S., Rignot, E.,  
936 Paden, J., and Makinson, K.: Heterogeneous melting near the Thwaites Glacier grounding line, *Nature*, 614, 471–  
937 478, <https://doi.org/10.1038/s41586-022-05691-0>, 2023.

938 Schoof, C.: Ice sheet grounding line dynamics: Steady states, stability, and hysteresis, *J. Geophys. Res.*, 112, F03S28,  
939 <https://doi.org/10.1029/2006JF000664>, 2007.

940 TopoToolbox: <https://www.mathworks.com/matlabcentral/fileexchange/50124-topotoolbox>, last access: 21 June 2023.

941 Seroussi, H., Nakayama, Y., Larour, E., Menemenlis, D., Morlighem, M., Rignot, E., and Khazendar, A.: Continued retreat of  
942 Thwaites Glacier, West Antarctica, controlled by bed topography and ocean circulation, *Geophysical Research  
943 Letters*, 44, 6191–6199, <https://doi.org/10.1002/2017GL072910>, 2017.

944 Shean, D. E., Joughin, I. R., Dutrieux, P., Smith, B. E., and Berthier, E.: Ice shelf basal melt rates from a high-resolution digital  
945 elevation model (DEM) record for Pine Island Glacier, Antarctica, *The Cryosphere*, 13, 2633–2656,  
946 <https://doi.org/10.5194/tc-13-2633-2019>, 2019.

947 [Smith, B. E., Gourmelen, N., Huth, A., and Joughin, I.: Connected subglacial lake drainage beneath Thwaites Glacier,  
948 West Antarctica, \*The Cryosphere\*, 11, 451–467, <https://doi.org/10.5194/tc-11-451-2017>, 2017.](https://doi.org/10.5194/tc-11-451-2017)

949 Smith, B. E., Adusumilli, S., Csatho, B. M., Felikson, D., Fricker, H. A., Gardner, A. S., Holschuh, N., Lee, J., Nilsson, J.,  
950 Paolo, F. S., Siegfried, M. R., Sutterley, T. C., and ICESat-2 Science Team: ATLAS/ICESat-2 L3A Land Ice Height,  
951 Version 5, <https://doi.org/10.5067/ATLAS/ATL06.005>, 2021.

952 Smith, B. E., Adusumilli, S., Csatho, B. M., Felikson, D., Fricker, H. A., Gardner, A. S., Holschuh, N., Lee, J., Nilsson, J.,  
953 Paolo, F. S., Siegfried, M. R., Sutterley, T. C., and ICESat-2 Science Team: ATLAS/ICESat-2 L3A Land Ice Height,  
954 Version 6, <https://doi.org/10.5067/ATLAS/ATL06.006>, 2023.

955 [Stubblefield, A. G., Wearing, M. G., and Meyer, C. R.: Linear analysis of ice-shelf topography response to basal  
956 melting and freezing, \*Proceedings of the Royal Society A: Mathematical, Physical and Engineering Sciences\*, 479,  
957 20230290, <https://doi.org/10.1098/rspa.2023.0290>, 2023.](https://doi.org/10.1098/rspa.2023.0290)

958 Studinger, M.: IceBridge ATM L1B Elevation and Return Strength, Version 2, <https://doi.org/10.5067/19SIM5TXKPGT>,  
959 2013.

960 Vaughan, D. G., Corr, H. F. J., Bindschadler, R. A., Dutrieux, P., Gudmundsson, G. H., Jenkins, A., Newman, T., Vornberger,  
961 P., and Wingham, D. J.: Subglacial melt channels and fracture in the floating part of Pine Island Glacier, Antarctica,  
962 *J. Geophys. Res.*, 117, F03012, <https://doi.org/10.1029/2012JF002360>, 2012.

963 Washam, P., Nicholls, K. W., Münchow, A., and Padman, L.: Summer surface melt thins Petermann Gletscher Ice Shelf by  
964 enhancing channelized basal melt, *Journal of Glaciology*, 65, 662–674, <https://doi.org/10.1017/jog.2019.43>, 2019.

965 Wearing, M. G., Stevens, L. A., Dutrieux, P., and Kingslake, J.: Ice-Shelf Basal Melt Channels Stabilized by Secondary Flow,  
966 *Geophysical Research Letters*, 48, e2021GL094872, <https://doi.org/10.1029/2021GL094872>, 2021.

967 Weertman, J.: Stability of the Junction of an Ice Sheet and an Ice Shelf, *Journal of Glaciology*, 13, 3–11,  
968 <https://doi.org/10.1017/S0022143000023327>, 1974.

969 van Wessem, J. M., van de Berg, W. J., Noël, B. P. Y., van Meijgaard, E., Amory, C., Birnbaum, G., Jakobs, C. L., Krüger,  
970 K., Lenaerts, J. T. M., Lhermitte, S., Ligtenberg, S. R. M., Medley, B., Reijmer, C. H., van Tricht, K., Trusel, L. D.,  
971 van Ulf, L. H., Wouters, B., Wuite, J., and van den Broeke, M. R.: Modelling the climate and surface mass balance  
972 of polar ice sheets using RACMO2 – Part 2: Antarctica (1979–2016), *The Cryosphere*, 12, 1479–1498,  
973 <https://doi.org/10.5194/tc-12-1479-2018>, 2018.

974 Wild, C. T., Alley, K. E., Muto, A., Truffer, M., Scambos, T. A., and Pettit, E. C.: Weakening of the pinning point buttressing  
975 Thwaites Glacier, West Antarctica, *The Cryosphere*, 16, 397–417, <https://doi.org/10.5194/tc-16-397-2022>, 2022.

976 Yu, H., Rignot, E., Seroussi, H., and Morlighem, M.: Retreat of Thwaites Glacier, West Antarctica, over the next 100 years  
977 using various ice flow models, ice shelf melt scenarios and basal friction laws, *The Cryosphere*, 12, 3861–3876,  
978 <https://doi.org/10.5194/tc-12-3861-2018>, 2018.

979 Zinck, A.-S. P., Wouters, B., Lambert, E., and Lhermitte, S.: REMA reveals spatial variability within the Dotson Melt Channel,  
980 *The Cryosphere Discussions*, 1–25, <https://doi.org/10.5194/tc-2023-14>, 2023.

981